Physics of Plasmas

Multi-scale evolution of Kelvin–Helmholtz waves at the Earth's magnetopause during southward IMF periods

Cite as: Phys. Plasmas **29**, 012901 (2022); https://doi.org/10.1063/5.0067391
Submitted: 16 August 2021 • Accepted: 21 November 2021 • Published Online: 06 January 2022

T. K. M. Nakamura, K. A. Blasl, H. Hasegawa, et al.

Physics of Plasmas ARTICLE scitation.org/journal/php

Multi-scale evolution of Kelvin–Helmholtz waves at the Earth's magnetopause during southward IMF periods

Cite as: Phys. Plasmas **29**, 012901 (2022); doi: 10.1063/5.0067391
Submitted: 16 August 2021 · Accepted: 21 November 2021 ·
Published Online: 6 January 2022

T. K. M. Nakamura,[1,2,a)] K. A. Blasl,[1,2] H. Hasegawa,[3] T. Umeda,[4] Y.-H. Liu,[5] S. A. Peery,[5] F. Plaschke,[2,6] R. Nakamura,[2] J. C. Holmes,[2] J. E. Stawarz,[7] and W. D. Nystrom[8]

AFFILIATIONS

[1]Institute of Physics, University of Graz, Graz 8010, Austria
[2]Space Research Institute, Austrian Academy of Sciences, Graz 8010, Austria
[3]Institute of Space and Astronautical Science, Japan Aerospace Exploration Agency, Sagamihara 252-5210, Japan
[4]Institute for Space-Earth Environmental Research, Nagoya University, Nagoya 464-8601, Japan
[5]Department of Physics and Astronomy, Dartmouth College, Hanover, New Hampshire 03755, USA
[6]Institute of Geophysics and extraterrestrial Physics, TU Braunschweig, Braunschweig 38092, Germany
[7]Department of Physics, Imperial College London, London SW7 2BW, United Kingdom
[8]HPC Division, Los Alamos National Laboratory, Los Alamos, New Mexico 87545, USA

Note: This paper is a part of the Special Collection: Plasma Physics from the Magnetospheric Multiscale Mission.
[a)]**Author to whom correspondence should be addressed:** takuma.tkm.nakamura@gmail.com

ABSTRACT

At the Earth's low-latitude magnetopause, the Kelvin–Helmholtz instability (KHI), driven by the velocity shear between the magnetosheath and magnetosphere, has been frequently observed during northward interplanetary magnetic field (IMF) periods. However, the signatures of the KHI have been much less frequently observed during southward IMF periods, and how the KHI develops under southward IMF has been less explored. Here, we performed a series of realistic 2D and 3D fully kinetic simulations of a KH wave event observed by the Magnetospheric Multiscale (MMS) mission at the dusk-flank magnetopause during southward IMF on September 23, 2017. The simulations demonstrate that the primary KHI bends the magnetopause current layer and excites the Rayleigh–Taylor instability (RTI), leading to penetration of high-density arms into the magnetospheric side. This arm penetration disturbs the structures of the vortex layer and produces intermittent and irregular variations of the surface waves which significantly reduces the observational probability of the periodic KH waves. The simulations further demonstrate that in the non-linear growth phase of the primary KHI, the lower-hybrid drift instability (LHDI) is induced near the edge of the primary vortices and contributes to an efficient plasma mixing across the magnetopause. The signatures of the large-scale surface waves by the KHI/RTI and the small-scale fluctuations by the LHDI are reasonably consistent with the MMS observations. These results indicate that the multi-scale evolution of the magnetopause KH waves and the resulting plasma transport and mixing as seen in the simulations may occur during southward IMF.

I. INTRODUCTION

The Kelvin–Helmholtz instability (KHI) becomes unstable when the plasma shear flow is super-Alfvénic for the magnetic field component parallel to the shear flow (Chandrasekhar, 1961). This unstable condition is easily satisfied when the magnetic field is oriented nearly perpendicular to the direction of the shear flow. At the Earth's low-latitude magnetopause, this magnetic field configuration appears when the interplanetary magnetic field (IMF) is strongly northward or southward. Indeed, clear signatures of surface waves and flow vortices, which could be generated by the KHI, have been frequently observed around the low-latitude magnetopause during periods of strong northward IMF (e.g., Sckopke *et al.*, 1981; Kokubun *et al.*, 1994; Slinker

et al., 2003; Kivelson and Chen, 1995; Fairfield et al., 2000; Hasegawa et al., 2004; 2006; Foullon et al., 2008; Kavosi and Raeder, 2015; Moore et al., 2016). These magnetopause KH waves and vortices have been believed to cause efficient mass, momentum, and energy transfer across the magnetopause and effectively contribute to forming the Earth's low-latitude boundary layer (LLBL), where plasmas of magnetosheath and magnetospheric origins are mixed, during the northward IMF periods (e.g., Nakamura, 2021 and references therein).

On the other hand, although the magnetopause boundary layer can be unstable for the KHI, even for the southward IMF in the MHD regime, as long as the magnetic field component parallel to the shear flow is weak enough (Chandrasekhar, 1961), the signatures of the magnetopause KH waves and vortices have been much less frequently observed during periods of southward IMF (e.g., Kavosi and Raeder, 2015). Hwang et al. (2011) reported a Cluster observation event of nonlinear KH vortices during a southward IMF period. In this event, observed plasma and field variations were irregular and temporally intermittent, indicating that the structure of the KH vortices was being disturbed. A recent three-dimensional (3D) fully kinetic simulation under pure southward IMF conditions demonstrated that strong evolution of magnetic reconnection across thin current layers formed within the KH waves quickly destroys the wave and vortex structures (Nakamura et al., 2020a). This reconnection-driven decay process of the KH vortex may explain the intermittent and irregular variations of the observed KH vortices as well as the low observational probability of the periodic KH waves/vortices during southward IMF. However, it was difficult to resolve the thin current layers and confirm the occurrence of the vortex-induced reconnection (VIR) in the reported Cluster event because of the insufficient time resolution in plasma measurements.

High-time-resolution fields and plasma data collected by the Magnetospheric Multiscale (MMS) mission (Burch et al., 2016) have been used to resolve small-scale physics within the KH waves and vortices, such as the VIR, as recently shown for some magnetopause KH wave events during the northward IMF (Eriksson et al., 2016a; 2016b; Li et al., 2016; Vernisse et al., 2016; Stawarz et al., 2016; Tang et al., 2018; Hasegawa et al., 2020; Hwang et al., 2020; Kieokaew et al., 2020). In these northward IMF events, signatures of the VIR, such as reconnection outflow jets (Eriksson et al., 2016a; Li et al., 2016), energy dissipation within the electron diffusion region (Eriksson et al., 2016b), turbulent spectra caused by turbulent evolution of the VIR (Stawarz et al., 2016; Hasegawa et al., 2020), and the formation of multiple flux ropes and their interactions (Hwang et al., 2020; Kieokaew et al., 2020) were reported. 3D fully kinetic simulations of one of these MMS events on September 8, 2015 showed that the simulated VIR signatures are reasonably consistent with many of the above observation signatures (Nakamura et al., 2017a; 2017b; Nakamura et al., 2020b; Nakamura, 2021). Although past theoretical and numerical studies suggested that the plasma shear flow can reduce the rate of spontaneous reconnection and weaken the resulting solar wind transport across the magnetopause (e.g., Cassak and Otto, 2011), these realistic simulations of the observed VIR further showed that the VIR, which is a strongly driven reconnection process controlled by the super-Alfvénic vortex flow and whose rate is much higher than that of spontaneous reconnection, leads to an efficient solar wind transport. Based on the consistencies between the observations and simulations, these studies indicated that the KHI and subsequent occurrence of the VIR would indeed contribute to efficient solar wind transport during northward IMF.

Based on these previous studies, our companion paper, Blasl et al. (unpublished), reported the first MMS observations of the KH waves during southward IMF. In this event, MMS observed the intermittent and irregular variations of the surface waves, which can be interpreted as being formed by the KHI during the southward IMF and magnetosheath magnetic field. Although clear VIR signatures as reported in the above MMS observation events for the northward IMF were not found in this event, the high-time-resolution measurements of MMS frequently detected small-scale fluctuations, which can be interpreted as being generated by the lower-hybrid drift instability (LHDI), excited near the edge of the surface waves. To investigate this event in more detail, in the present paper, we perform a series of 2D and 3D fully kinetic simulations with parameters matched to this MMS event. The simulation results are consistent with the observations in terms of both large-scale surface wave signatures and small-scale LHDI fluctuations. The simulations also demonstrate that the primary KH waves induce the secondary Rayleigh–Taylor instability (RTI) at the surface bent by the KHI. The RTI forms high-density arms penetrating into the low-density magnetospheric side. This arm penetration quickly disturbs the primary KH wave structures and produces intermittent and irregular variations of the surface waves, leading to a reduction in the observational probability of the primary KH waves. Interestingly, this RTI-related reduction of the observational probability of the KH waves proceeds faster than the above VIR-related reduction for the northward IMF, indicating that the secondary RTI may also be a key process that makes it more difficult to detect the KH waves during southward IMF.

This paper is organized as follows. Section II describes the details of the simulation model employed in this paper. Section III presents the overall simulation results focusing on the large-scale variations of the surface waves, while in Sec. IV we focus on the secondary processes induced within the primary waves. In Sec. V, we summarize the results and discuss differences in the evolution of the KH waves between the northward and southward IMF conditions.

II. MODEL

A. Simulation settings

We performed a series of 2D (in the x–y plane) and 3D fully kinetic simulations that model a magnetopause crossing event observed by MMS on September 23, 2017 [Blasl et al. (unpublished)], using the high-performance particle-in-cell code VPIC (Bowers et al., 2008; 2009). The x, y, and z coordinates in the simulations correspond to the direction along the velocity shear (∼the magnetosheath flow in the equatorial plane), the boundary normal (∼magnetosheath-to-magnetosphere), and the out-of-the-vortex-plane (∼south-to-north), respectively. The initial density, magnetic field, and ion (and electron) bulk velocities across the magnetopause boundary layer are set to the values obtained from the observations near the KH vortex-like interval 15:33–15:35 UT [see Blasl et al. (unpublished) for more details of this interval]. Denoting the magnetosheath and magnetospheric sides as 1 and 2, respectively, we first select the density (n_{10}, n_{20}), the magnetic field (B_{x10}, B_{z10}, B_{x20}, B_{z20}), and the bulk velocities (U_{x10}, U_{z10}, U_{x20}, U_{z20}) on the two sides from the observations. To set the initial equilibrium, we here neglect the y-component of the initial magnetic field and velocities, which are negligibly small compared to the x and z components. We then set the initial density profiles by connecting these values across the magnetopause using a $\tanh(y/L_0)$ function

(Nakamura and Daughton, 2014) as $n_1(y) = \frac{n_{10}}{2}\left[1 - \tanh\left(\frac{z}{L_0}\right)\right]$ and $n_2(y) = \frac{n_{20}}{2}\left[1 + \tanh\left(\frac{z}{L_0}\right)\right]$, where $L_0 = 2.5d_i$ is the initial half thickness of the shear layer and $d_i = c/\omega_{pi}$ is the ion inertial length based on $n_0 = n_{10}$. To set the bulk velocities, particles (ions and electrons) are initialized with drifting Maxwellian velocities whose drift velocities are U_{x10} and U_{x20} for the magnetosheath and magnetospheric particles, respectively. The initial magnetic field is setup as $B_{x,z}(y) = \frac{B_{x,z10}}{2}\left[1 - \tanh\left(\frac{y}{L_0}\right)\right] + \frac{B_{x,z20}}{2}\left[1 + \tanh\left(\frac{y}{L_0}\right)\right]$. Additional electron and ion flows and electron density are introduced to satisfy the Harris type variation of B_x and B_z. To satisfy the force balance, the temperatures for the magnetospheric ion and electron components $T_{i,e20}$ are set to be higher than the magnetosheath components $T_{i,e10}$, where the ion-to-electron temperature ratio is fixed as $T_{i0}/T_{e0} = 5.0$.

The set of values obtained from MMS data in regions 1 and 2 are $n_{10}/n_{20} = 8.0$, $B_{z10} = -B_0$, $B_{z20} = B_0$, $U_{x10} = V_0/2$, and $U_{x20} = -V_0/2$, where $n_{10} = 8\,cm^{-3}$, $B_0 = 12$ nT, $|V_0| = 290$ km/s $= 3.0V_A$ (V_A: Alfvén speed based on n_0 and B_0). Note that the system is set to be in a drifting frame of reference with half the velocity of the magnetosheath flow. Since the in-plane magnetic field components (B_{x10} and B_{x20}) are known to easily change within the vortex layer as a result of the vortex motion (e.g., Fairfield *et al.*, 2007; Nakamura *et al.*, 2008), it is difficult to determine B_{x10} and B_{x20} from the observations during the vortex-like fluctuating interval. Nevertheless, since the spacecraft crossed a relatively steady magnetosheath-like interval just before the vortex-like interval, we took B_{x10} from this interval as 0.17–$0.2B_0$. Regarding B_{x20}, since the spacecraft did not cross a clear magnetosphere-like region near the vortex-like interval, we tested various values from 0 to $0.2B_0$. In this paper, we show representative simulation runs with (B_{x10}, B_{x20}) $= (0.2B_0, 0)$ and $(0.17B_0, 0.17B_0)$ (i.e., a case with no in-plane field on the magnetospheric side and a case with uniform in-plane field) as listed in Table I. The total plasma beta on the magnetosheath side is $\beta_1 = 1.5$, the ratio between the electron plasma frequency and the gyrofrequency is $\omega_{pe}/\Omega_e = 2.0$ and the ion-to-electron mass ratio is $m_i/m_e = 100$ for all runs. The system is periodic in x (and in z for 3D), and y boundaries are modeled as perfect conductors for the fields and reflecting for the particles.

In this paper, we will show the results from four runs listed in Table I. We will first show a large-scale 2D run (run-A), in which the system size is $L_x \times L_y = 100d_i \times 100d_i = 6144 \times 6144$ cells with a total of 1.5×10^{10} (super)particles. In this run, we added no specific mode of initial perturbations and the KH instability grows from the random particle noises. Then, to investigate the three-dimensional effects, we will show local 3D (run-B) and 2D (run-C) runs, which feature one wavelength KH mode ($m_x = 1$) with the system size $L_x \times L_y \times L_z = 15d_i \times 30d_i \times 10.4d_i = 864 \times 1728 \times 600$ cells with a total of 3.6×10^{11} particles for 3D, and $L_x \times L_y = 15d_i \times 30d_i = 864 \times 1728$ cells with a total of 6.0×10^9 particles for 2D. In these local runs, to initiate the one wavelength KH mode, we added an initial weak flow perturbation as $\delta U_{iy} = \delta U_{ey} = 0.02V_0\exp[-0.5(y/L_0)^2]\sin(2\pi x/L_x)$. In addition, to investigate the effects of the in-plane magnetic field, we will also show a local 2D run (run-D) with the same setting as run-C except that the in-plane field is initially set to be zero. Note that for the 3D run (run-B), which used $\sim 2 \times 10^4$ cores of MareNostrum at Barcelona Supercomputing Center (BSC) for more than 10^2 h, we setup the largest system size within the computer resource limitation to reproduce the MHD-scale ($>d_i$) primary KH waves without being affected by non-MHD effects in their initial growth phase, although the size is still about ten times smaller than the estimated wavelength ($\lambda_{KH} \sim 10^{4-5}$ km $\sim 10^{2-3}$ d_i) of the KH waves in the MMS observations [Blasl *et al.* (unpublished)].

B. Initial equilibrium

In the present simulations, the pressure balance in the boundary normal (y) direction is satisfied in the initial conditions. However, when the magnetic field strength within the current layer is significantly weaker than that in the outside regions like the Harris-type current sheet as employed in the present simulations, the fluid-type equilibrium across the layer is easily disturbed by kinetic effects. One of the main causes for this disturbance is the gyro-motion of ions located near the center of the layer. The orbits of these ions are larger due to the smaller magnetic field within the layer. As the simulation proceeds, the simulated particles start their gyro-motions and the orbits of the ions that initially located near the center but on one side of the layer can enter the other side of the layer because of the finite gyro-radius. When there is initially a large density jump across the layer as in the present simulations, the net number of the crossing ions that originally located on the two sides is not balanced, leading to the disturbance of the equilibrium. Figure 1 shows the time evolutions of the 1D profiles in the y direction of the ion density, the out-of-plane magnetic field component, and the shearing flow component for the large-scale 2D run (run-A). As the simulation proceeds, the high-density plasma penetrates into the lower-density side as predicted. After a few ion gyro-periods, a new quasi-equilibrium state, in which the profiles are no longer largely changed, is accomplished. Note that the KH instability starts to grow after this new equilibrium is accomplished, as will be shown in Fig. 2 and Sec. III.

TABLE I. Key differences among simulation runs employed in this paper.

Run	A	B	C	D
2D or 3D	2D	3D	2D	2D
System size (d_i)	100×100	$15 \times 30 \times 10.4$	15×30	15×30
In-plane field (B_0)	B_{x10}:0.2 B_{x20}:0.0	B_{x10}:0.17 B_{x20}:0.17	B_{x10}:0.17 B_{x20}:0.17	B_{x10}:0.0 B_{x20}:0.0
Potential secondary processes	RTI LHDI	RTI LHDI reconnection	RTI	RTI LHDI

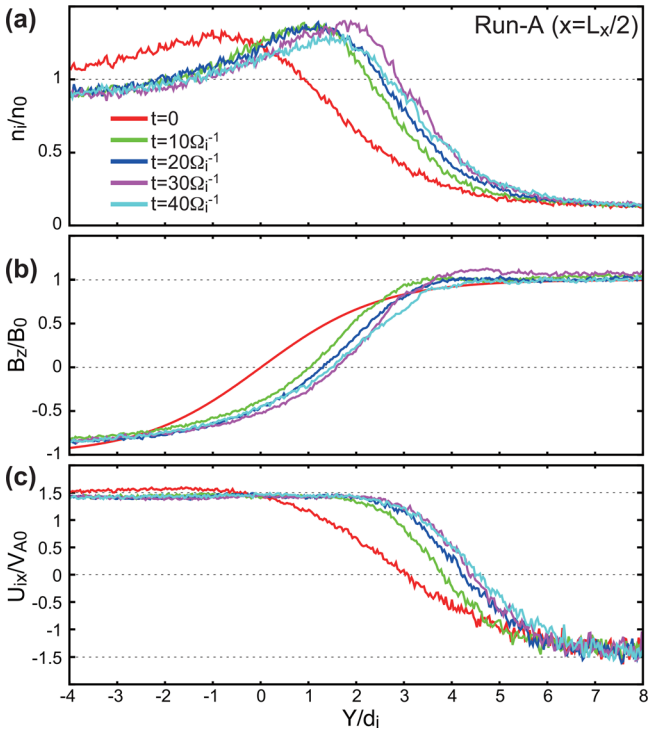

FIG. 1. Time evolution of the profiles in the y-direction at $x = L_x/2$ for the large-scale 2D run (run-A) of (a) the ion density n_i, (b) the out-of-plane component of the magnetic field B_z, and (c) the x-component of the ion bulk velocity U_{ix} from $t = 0$ to 40 Ω_i^{-1}.

III. LARGE-SCALE EVOLUTION OF KH WAVES

A. Overview of the simulation results

Figures 2(a)–2(d) show the time evolution of the ion density for run-A. At $t = 50\ \Omega_i^{-1}$, we see that 6 KH waves are growing near the center of the boundary layer [Fig. 2(a)]. After that, a part of the surface waves, which convects toward the low-density side, grows as high-density arms penetrating into the low-density side [Figs. 2(c) and 2(d)]. Notice that although the arms start to roll-up a small amount, they mainly continue to grow more straight into the low-density side beyond the vortex layer and greatly disturb the layer structure. Notice also that the width of the high-density arms tends to become smaller over time as they grow in the boundary normal direction. Figure 2(e) shows the growth of the 1D power spectra (k_x) of each U_{iy} modes. We show that in the early phase until $t \sim 50$–$60\ \Omega_i^{-1}$, the $m_x = 6$ mode clearly dominates, but after that the relative power of the other modes relatively gets larger corresponding to the evolution of the high-density arms, and it becomes more difficult to identify one dominant mode. As will be described in detail in Sec. IV A, this additional evolution of the high-density arms is caused by the Rayleigh–Taylor instability (RTI) driven by the centrifugal force at the rippled surface.

In addition, as the large-scale surface waves develop, smaller-scale fluctuations grow, especially near the edges of the waves where the density gradient is enhanced [see, for example, a white arrow in Fig. 2(a)]. These fluctuations are seen mainly on the low-density side of the gradient layer and penetrate deep into the lower-density region.

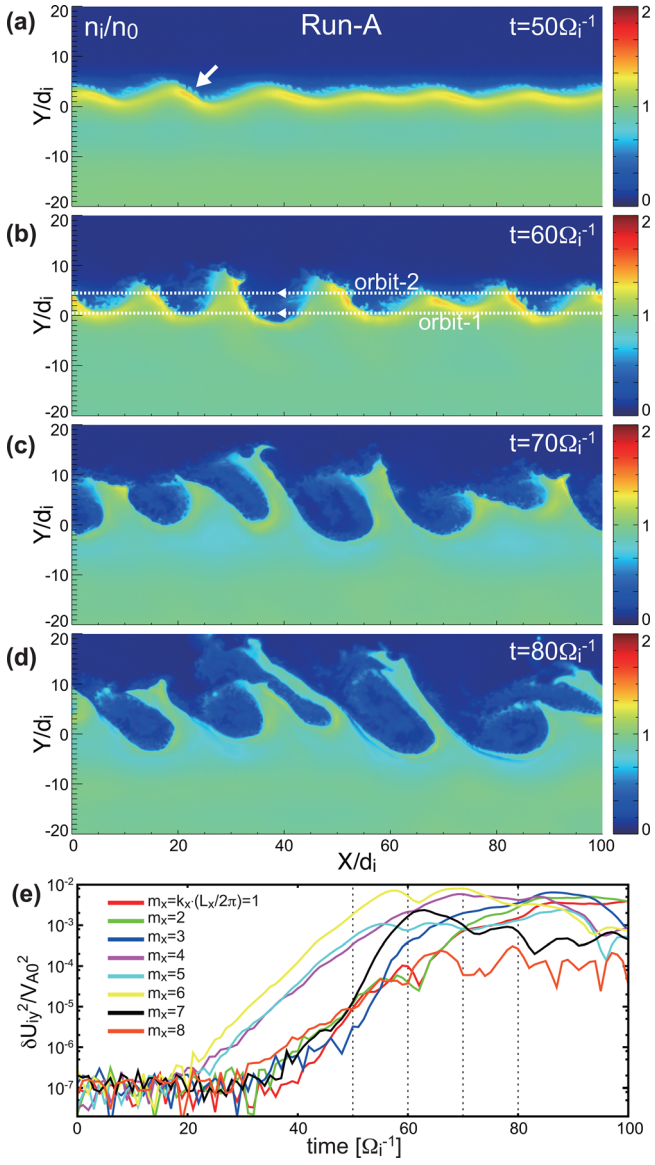

FIG. 2. (a)–(d) Time evolution of color contours of n_i in the x–y plane from $t = 50$ to 80 Ω_i^{-1} for run-A. (e) Time evolution of the 1D power spectra (k_x) of U_{iy} modes ($m_x = 1$ to $m_x = 8$) around the center of the boundary ($y = 0 \pm 8.3 d_i$). Vertical lines indicate the times shown in (a)–(d).

As a result of the fluctuations, the gradient layer, where plasmas between the two sides across the layer are mixed, is substantially broadened near the edges of the RTI arms. As will be described in detail in Sec. IV B, these fluctuations result from the lower-hybrid drift instability (LHDI) driven by the thin density gradient layer formed at the edge of the primary surface waves/vortices.

B. Comparison with the MMS observations

To confirm the realism of the simulation, we compare the simulation results with the MMS observations of the large-scale evolution

of the KH waves. Figures 3(a)–3(h) show the virtual observations along the orbits-1 and 2 marked in Fig. 2(b), while Figs. 3(i)–3(l) show the MMS observations during 15:30–16:30 UT on September 23, 2017. In the virtual observations, we assume that the spacecraft crossed the vortex layer in the direction opposite to the propagation direction of the KH waves (i.e., −x direction) at a fixed time around the transition between the linear and non-linear growth phase of the KHI ($t = 60\ \Omega_i^{-1}$). Orbit-1 crossed near the magnetosheath side edge of the bulges of the primary KH waves and vortices, while the orbit-2 crossed near the center part of the waves and vortices. For orbit-2 [Figs. 3(e)–3(h)], we clearly see regular patterns of the KH waves in which the density enhancement aligns with the positive to negative B_L (= B_z) oscillation, and the minimum U_N and maximum P_t are seen near the start point of these density and B_L variations [see the variations near the vertical line in Figs. 3(e)–3(h)]. For the orbit-1, these variations of the KH waves cannot clearly be seen, especially for the pressure [Fig. 3(d)], and instead a clear density drop aligns with positive B_L and U_N peaks [see the variations near the vertical line in Figs. 3(a)–3(d)].

Interestingly, variations similar to the virtual observations of both orbits-1 and 2 are seen in the MMS observations shown in Figs. 3(i)–3(l). During this one-hour interval, MMS repeatedly encountered positive–negative variations of B_L accompanied by density variations, indicating multiple encounters of the magnetopause surface waves or the oscillations of the magnetopause in the boundary normal directions. The observed variation patterns of the boundary normal vectors at these density changes strongly suggest that these variations were most likely caused by the surface waves [see Fig. 3 in Blasl *et al.* (unpublished)]. During the early part of this interval, MMS observed the high-density plasmas for a longer time, while at a later time, MMS observed the low-density plasmas for a longer time and more frequently encountered wave-like repeated variations, indicating that the spacecraft moved from the magnetosheath side toward the center of the layer where the surface waves were active. The variation patterns of the density, B_N, V_N, and P_t during the early and later intervals are quantitatively consistent with the virtual observations for the orbits-1 and 2 in the normalized units of the simulation ($B_0 = 12$ nT, $n_0 = 8\ \mathrm{cm}^3$), respectively [compare the variations near the blue vertical line in Figs. 3(a)–3(d) and the green vertical line in Figs. 3(e)–3(h) and those near the blue and green vertical lines in Figs. 3(i)–3(l), respectively]. Furthermore, given the averaged V_N during 15:40–16:00 UT (the transition between the early and later intervals) $\langle V_N \rangle \sim +9.5$ km/s, and assuming that the magnetopause moved toward the magnetosheath side in the boundary normal direction at this speed, it is inferred that the spacecraft relatively moved about 10^4 km toward the magnetospheric side during 15:40–16:00 UT. Since the estimated wavelength of the observed surface waves is about 5×10^4 km, this distance

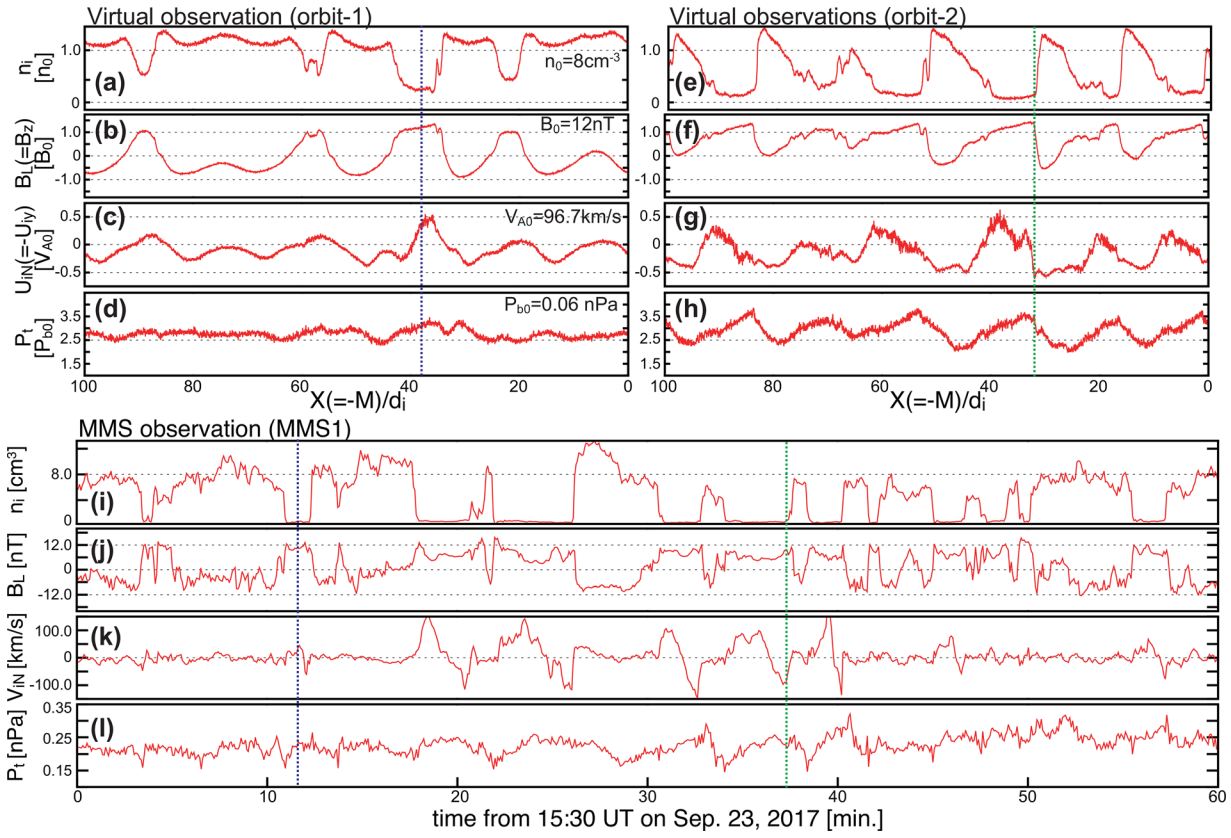

FIG. 3. (a)–(h) Virtual observations of the KH waves for run-A, made along the orbits-1 and 2 shown in Figs. 2(b) and (i)–(l) the *in situ* observations by the MMS1 spacecraft for 1 h from 15:30 UT of the ion density, L (= z) component of the magnetic field, N (= −y) component of the ion bulk velocity and the total pressure. The time interval in (i)–(l) is the same as the one in Fig. 3 in Blasl *et al.* (unpublished).

corresponds to $\sim 1/5\lambda_{KH}$, which is roughly consistent with the distance between the orbits-1 and 2 in the boundary normal direction ($3d_i \sim 1/5\lambda_{KH}$). We have confirmed that similar consistencies between the simulation and observations are seen in a range $t \sim 60$–$65\ \Omega_i^{-1}$ (i.e., near the later linear or early non-linear growth phase of the KHI). All of these consistencies indicate that the KH waves near the later linear or early non-linear growth phase as seen in the present simulation at $t = 60\ \Omega_i^{-1}$ likely occur at the dusk-flank magnetopause during this interval. Note that we see the low-density and negative B_L values more frequently and for a longer time after the crossing of the green vertical line in Figs. 3(i)–3(l), indicating that the spacecraft moved deeper into the magnetosphere. See Blasl *et al.* (unpublished) for more details of the comparisons between the present simulation and MMS observations.

IV. SECONDARY INSTABILITIES

A. Secondary RTI

To investigate the evolution process of the KHI and the subsequent secondary processes in more detail, we performed local 2D and 3D runs featuring one wavelength KH mode with a similar wavelength ($15d_i$) to the fastest growing mode seen in run-A (listed as runs-B and C in Table I, respectively). In these runs, the in-plane field is initially set to be uniform. Figures 4(a)–4(d) show the time evolution of the ion density contours for the 2D run (run-C). As also seen in Fig. 2, for run-A, the high-density arm penetrates deep into the low-density side, and the arm becomes narrower as the head of the arm propagates in the y direction. The growth rate of the arm, which is roughly reflected by $m_x = 2$ or 3 at least at the beginning of the arm growth as will be shown in Fig. 5 and the next paragraph, is larger than the growth rate of the primary KHI with $m_x = 1$ [compare the slopes of the curves in Fig. 4(e)]. After the rapid growth of the arm [see $t > 5\alpha^{-1}$ in Fig. 4(e)], the amplitude of the parent KH mode ($m_x = 1$) is substantially reduced down to the level comparable to the $m_x = 2 + 3$ modes (the sum of the amplitudes of $m_x = 2$ and 3 modes).

Figures 5(a)–5(e) feature the evolution of the high-density arm during $t = 3.2\alpha^{-1}$ to $5.6\alpha^{-1}$, where $\alpha^{-1} = \lambda_{KH}/V_0$ is the time unit for the growth phase of the KHI (Nakamura *et al.*, 2013). As mentioned above, the width of the arm becomes smaller as the arm grows in the boundary normal direction. As highlighted by the yellow curves in Figs. 5(a) and 5(b), this corresponds to the decrease in the curvature radius of the head of the high-density arm. The ratio of the radius between $t = 3.2\alpha^{-1}$ and $3.8\alpha^{-1}$ is about 1.7^{-1}, and this number is consistent with the inverse of the square of the ratio of the growth rate of the $m_x = 2 + 3$ mode between $t = 3.2\alpha^{-1}$ to $3.8\alpha^{-1}$ [see Fig. 5(f)]. Here, the $m_x = 2 + 3$ mode roughly corresponds to the width of the arm in the x direction (i.e., the width of the arm is roughly 0.3–0.5 times the wavelength of the primary KH mode) during this time interval. Within this curved boundary layer, the current, which is produced by the anti-parallel south-to-north magnetic field across the layer and is mainly carried by ions, flows in the direction along the layer [see arrows in Figs. 5(a)–5(e)]. Given that the strength of the current near the density surface stays almost the same between $t = 3.2\alpha^{-1}$ to $3.8\alpha^{-1}$, the relation between the curvature radius and growth rate of the head is consistent with the expected growth rate of the RTI excited by the centrifugal force from the curved flow (Chandrasekhar, 1961; Nakamura and Daughton, 2014); $\gamma_{RT} \propto \left(U_r^2/r\right)^{0.5}$, where U_r is the rotating flow speed and r is the curvature radius of the flow. After the saturation of the $m_x = 2 + 3$ mode, the mushroom-like structure forms near the head of the arm [see white arrows in Figs. 5(e) as well as 4(c)], supporting that the RTI is secondarily induced at the density surface bent by the primary KHI, and forms the high-density arm penetrating into the low-density side. It should be emphasized here that since the current flows in the direction largely tilted from the KHI plane ($\sim$ the equatorial plane) for the northward IMF case, this RTI physics would be unique for the southward IMF case in which the current flows nearly along the background shear flow.

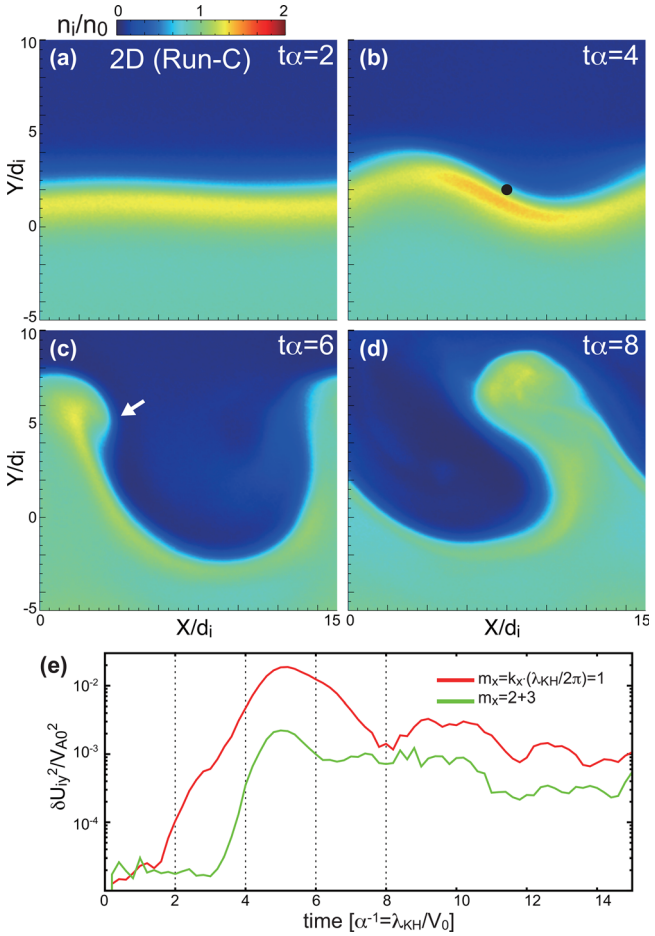

FIG. 4. (a)–(d) Time evolution of color contours in the x–y plane of n_i from $t = 2$ to $8\alpha^{-1}$ for the local 2D run (run-C), where $\alpha^{-1} = \lambda_{KH}/V_0$ is the time unit for the growth phase of the KHI (Nakamura *et al.*, 2013). (e) Time evolution of the 1D power spectra (k_x) of U_{iy} modes ($m_x = 1$ and $m_x = 2 + 3$) obtained by calculating the power of each mode at each y and then picking up the maximum value for each mode. Vertical dotted lines in (e) indicate the times shown in (a)–(d).

B. 3D effects

Figures 6(a)–6(f) show the time evolution of the ion density and the x-component of the electric field in the electron frame $E'_x = (\boldsymbol{E} + \boldsymbol{U}_e \times \boldsymbol{B})_x$ for the local 3D run (run-B) in the x–y plane at $z = 0$. Similar to the 2D case in the x–y plane (see Fig. 4), the high-density arm penetrates into the low-density side, and the size of the

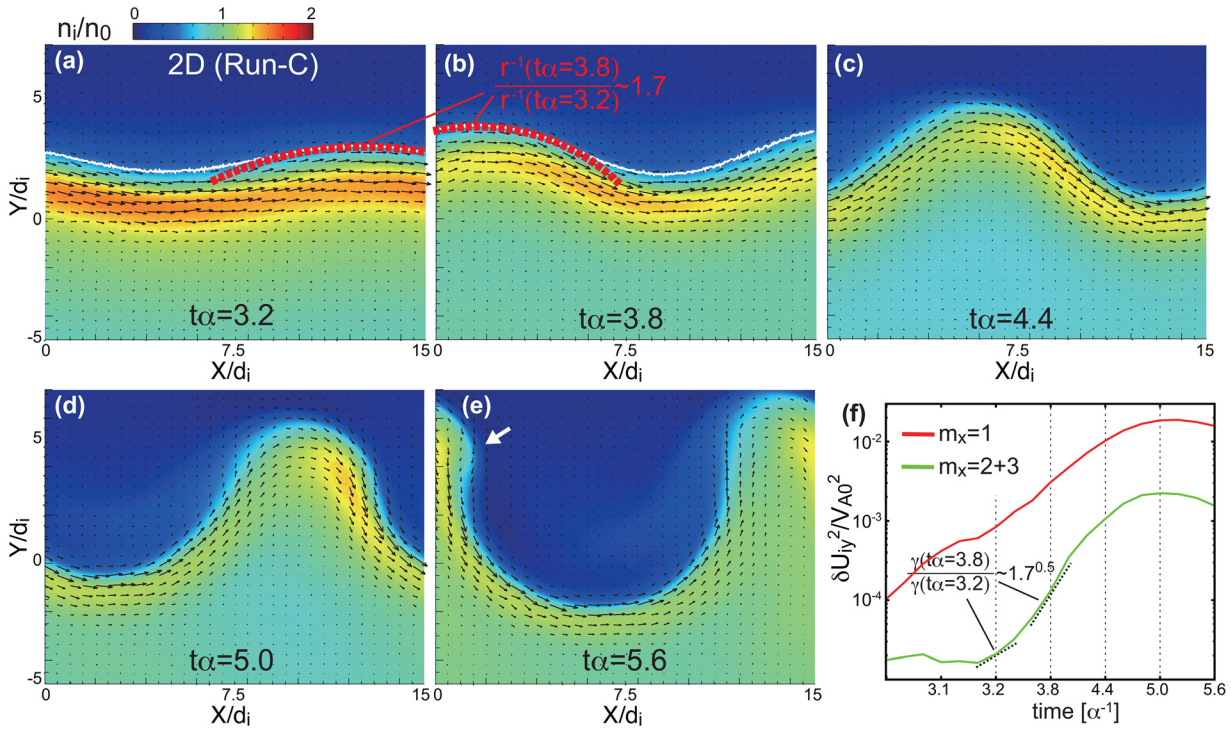

FIG. 5. (a)–(e) Time evolution of n_i contours for run-C from $t = 3.2$ to $5.6\alpha^{-1}$. Arrows show the in-plane components of the current density. The white and red dashed curves in (a) and (b) show the density surface with $(n_{10} + n_{20})/2$ and a portion of the fitted circles near the top of the primary wave structures, respectively. *r* in (a) and (b) indicate the curvature radius for the yellow curves. (f) Time evolution of the 1D power spectra (k_x) of U_{iy} modes $m_x = 1$ and $m_x = 2 + 3$. Vertical lines indicate the times shown in (a)–(e).

arm head decreases as the head moves deeper into the low-density side. However, as shown in Fig. 6(g), in the 3D case, the high-density arm grows in the direction somewhat tilted from the x–y plane (vortex plane), forming a large-scale wavy structure of the arm head in the z-direction (i.e., finite k_z is produced). This tilt angle corresponds to the direction perpendicular to the magnetic field measured at the arm head, as shown in Fig. 6(h). These features are consistent with the 3D evolution of the RTI in the direction satisfying $\boldsymbol{k} \cdot \boldsymbol{B} \sim 0$ in which the growth rate of the RTI is maximized (Chandrasekhar, 1961). Note that in Fig. 6(h) we also see a weak enhancement of the wave power at around $k_x \sim 10$–20, which reflects the small-scale fluctuations generated by the LHDI as will be explained in the next paragraph.

In the 3D case, it is also notable that small-scale fluctuations of the electric field, which are dominantly seen in the perpendicular components, grow mainly on the low-density side of the density gradient layer, as seen in Figs. 6(d)–6(f). These small-scale electric field fluctuations produce corresponding density fluctuations and broaden the low-density side of the layer [compare Figs. 6(a)–6(c) and 6(d)–6(f)]. The amplitude of the fluctuations is locally enhanced in the thin gradient layer compressed by the non-linearly developed primary surface wave and vortex [see the right-side of the edge layer of the primary wave/arm in Figs. 6(d)–6(f)]. The 3D view of the density surface in Fig. 6(g) shows that the wavy patterns of the small-scale density fluctuations are nearly aligned with the local magnetic field lines, indicating that the wavevector of the fluctuations develops in the direction nearly perpendicular to the local magnetic field. This point is clearly seen in the power spectrum at $t = 4\alpha^{-1}$ [Fig. 7(a)]. The power of the electric field fluctuations is enhanced dominantly in the direction nearly perpendicular to the mean magnetic field near the low-density side of the density gradient layer [$k_z/k_x \sim \tan(\theta_{perp})$], which roughly corresponds to the direction perpendicular to the local magnetic field in the region where the fluctuations are enhanced. As seen in the red curve in Fig. 7(c), the most strongly growing mode of the small-scale fluctuations at $t = 4\alpha^{-1}$ is $m_x \sim 18$–23 corresponding to the wavelength ~ 6.5–$8\ d_e$ in the x direction. Figure 7(d) shows the zoomed-in-view in the x–y plane of E_x' in the region marked in Fig. 6(d), where the fluctuations occur most strongly. The positive–negative pattern of the fluctuations whose projected wavelength in the x direction is around $7d_e$ is seen as expected from the power spectrum. The tilt angle of the edge layer in the x–y plane is about $\theta_{edge} \sim 35°$, indicating that the actual wavelength of the dominant mode is around $\lambda \sim 8.0$–$9.5\ d_e$, which is in a range of the hybrid-kinetic scale based on the local ion and electron temperatures and the magnetic field strength $[k_\perp(\rho_i\rho_e)^{1/2} \sim 1.4$–$1.7]$. The power spectrum [Fig. 7(c)] also shows that the enhanced power of the fluctuations spreads nearly up to the electron kinetic scale ($k_\perp \rho_e \sim 1$ corresponding to $m_x \sim 50$–55). These features (the perpendicular electric field fluctuations consisting of modes from the hybrid-kinetic to electron kinetic scales) are consistent with the ones predicted from the past linear analyses for the LHDI (Daughton, 2003). In the later time [see Fig. 7(b)], the in-plane magnetic field is more strongly compressed near the edge of the vortex/high-density arm, leading to θ_{perp} being larger and the strong power

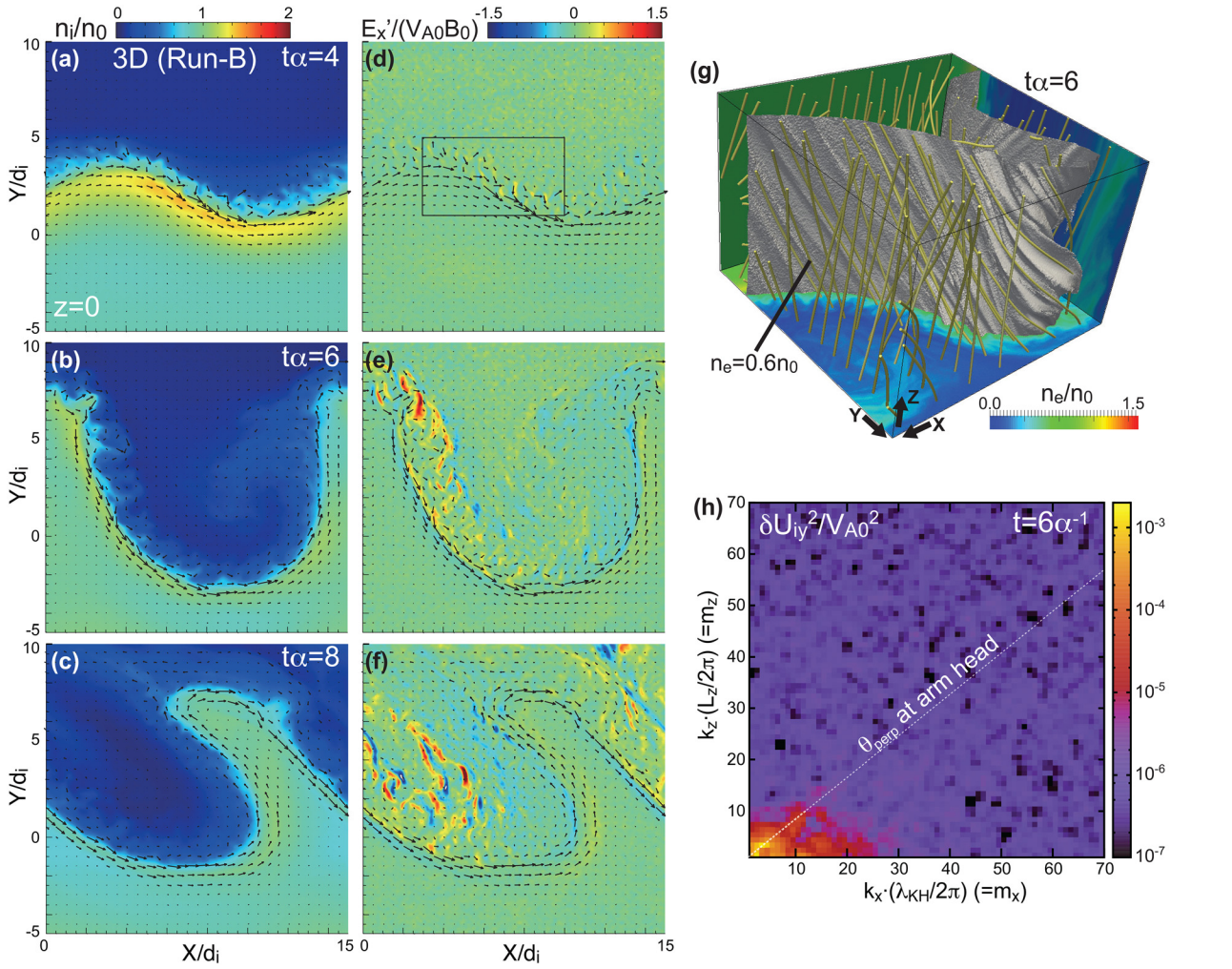

FIG. 6. (a)–(f) Time evolution of color contours of n_i (left) and the x-component of the electric field in the electron frame $E_x' = (\boldsymbol{E} + \boldsymbol{U}_e \times \boldsymbol{B})_x$ (right) from $t = 2$ to $8\alpha^{-1}$ (the same time interval as Fig. 4) for the local 3D run (run-B) at $z = 0$. Arrows show the in-plane components of the current density. (g) 3D view of the electron density surface of $n_e = 0.6n_0$ at $t = 6\alpha^{-1}$ for run-B with the electron density contours in the x–y plane at $z = 0$, x–z plane at $y = 0$, and y–z plane at $x = 0$ and randomly distributed magnetic field lines. (h) 2D power spectra (k_x, k_z) of U_{iy} at $t = 6\alpha^{-1}$ around the center of the boundary ($y = 0 \pm 5d_i$) for run-B. The dotted line indicates the angle of the perpendicular direction to the magnetic field in the x–z plane θ_{perp} at the head of the high-density arm.

seen more widely within the range $k_z/k_x < \tan(\theta_{perp})_{max}$. Notice that as the peaks are scattered, the wavelength of the most strongly growing mode becomes somewhat (1.5–2 times) longer [see the blue curve in Fig. 7(c)].

To understand the onset condition of these small-scale modes more quantitatively, a linear dispersion relation solver for fully kinetic plasma with a perpendicular drift, which has recently been developed in Umeda and Nakamura (2018), is applied by inputting parameters obtained from the simulation. In this solver, the dispersion relation is derived in the electromagnetic and fully kinetic regime for ions and electrons that drift in the direction perpendicular to the magnetic field, which can include ion and electron cyclotron resonances unlike the conventional approximation by Davidson *et al.* (1977) [see Umeda and Nakamura (2018) for more details about this linear dispersion relation]. This solver requires m_i/m_e and local values of the ion-to-electron temperature ratio T_i/T_e, ω_{pe}/ω_{ce}, the ion and electron drift velocities relative to the thermal speeds V_d/V_t, and the ratio between the thermal speeds and the speed of light V_t/c for ions and electrons as input parameters to obtain the dispersion relation. Figure 7(f) shows the results of the linear analysis in which the input parameters are obtained as local values at the location marked in Fig. 4(b). Note that the parameters are obtained at the location where the small-scale fluctuations are most strongly seen in the 3D run (run-B) but from the corresponding 2D run (run-C) in which the fluctuations are suppressed and thus we can obtain stable background values. The obtained parameters are $m_i/m_e = 100$, $T_i/T_e = 3.7$, $\omega_{pe}/\omega_{ce} = 1.8$, $V_{di}/V_{ti} = 0$, $V_{de}/V_{te} = 0.16$, $V_{ti}/c = 0.05$, and $V_{te}/c = 0.26$ ($\beta \sim 2.1$). The dispersion relation demonstrates that a quasi-perpendicular wave mode with a wave normal angle of $\phi \sim 87°$ relative to the ambient magnetic field has the maximum growth rate $\gamma \sim 0.06\omega_{LHR}$ at a wave number $m_{LH} = k_\perp(\rho_i\rho_e)^{1/2} \sim 1.6$, where

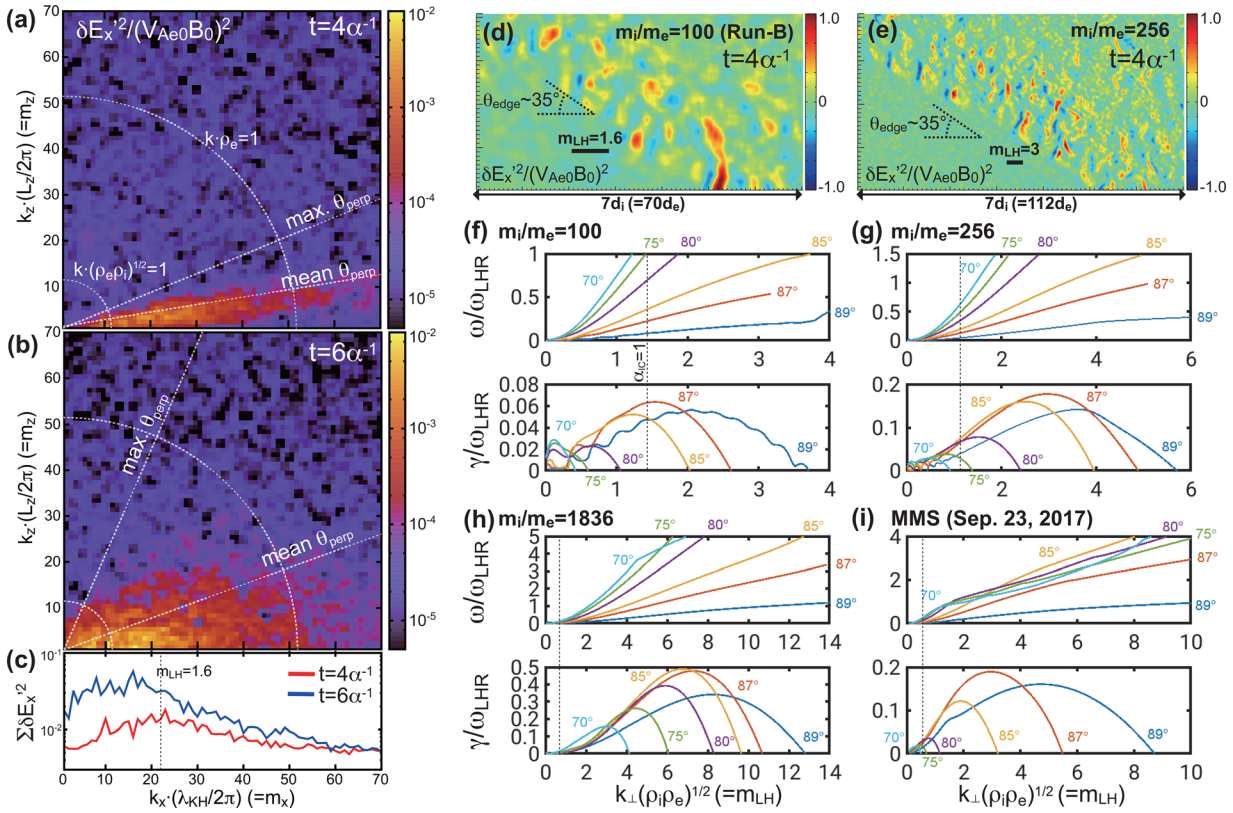

FIG. 7. (a)–(c) 2D power spectra (k_x, k_z) of E_x' and sum of the spectra in k_z at $t = 4$ and $6\alpha^{-1}$ around the center of the boundary ($y = 0 \pm 5d_i$) for run-B. The dotted lines in (a) and (b) indicate the angle of the perpendicular direction to the magnetic field in the x–z plane θ_{perp} at the head of the high-density arm, the maximum and mean θ_{perp} on the low-density side of the density gradient layer defined as the region with $0.2 < n_e/n_0 < 0.4$, and the wavelengths for $k_\perp\rho_e = 1$ and $k_\perp(\rho_i\rho_e)^{1/2} = 1$. (d) The zoomed-in view of the E_x' contour in the region marked in Fig. 6(d). (e) The same as (d), but for an additional run with $m_i/m_e = 256$. (f)–(i) Linear dispersion relations at the edge of the KH waves derived by Umeda and Nakamura (2018). Panels show wave modes with wave normal angles quasi-perpendicular to the ambient magnetic field ($\phi = 70^\circ - 89^\circ$) for parameters, obtained from the simulation near the compressed density gradient layer at $t = 4\alpha^{-1}$ marked in Fig. 4(b) (f), similar to (f) but for $m_i/m_e = 256$ (g) and $m_i/m_e = 1836$ (h), and obtained from the MMS observations on September 23, 2017 Blasl *et al.* (unpublished).

ω_{LHR} is the lower-hybrid frequency. Considering the tilt angle of the gradient layer in the x–y plane $\theta_{edge} \sim 35^\circ$ as discussed above, the dominant mode seen in the simulation is in excellent agreement with the fastest growing mode obtained from the linear analysis as seen in the red curve in Fig. 7(c). This clearly indicates that the $E_\perp$ fluctuations seen in the simulation are caused by the perpendicular plasma drifts and the related growth of the LHDI.

Notice that the dispersion relation for a mode with $\phi \sim 89^\circ$ in Fig. 7(f) shows a significantly low frequency below the ion cyclotron frequency ($<0.1\omega_{LHR}$), which indicates that some modes could be largely affected by the ion gyro-motion in the present simulation. This could be because when the ion-to-electron mass ratio is low, as in the present simulation ($m_i/m_e = 100$), the gyro-radius of a large portion of ions can be comparable to or smaller than the wavelength of the electric field fluctuations (i.e., hybrid-kinetic scale), and hence their motions can largely affect the evolution of the waves in addition to electron motions. For example, in the present case, the ratio between the ion gyro-radius and the wavelength of the fluctuations $\alpha_{IC} = \rho_i/[2\pi(\rho_i\rho_e)^{1/2}/m_{LH}] = (m_{LH}/2\pi) \cdot (m_i/m_e)^{1/4} \cdot (T_i/T_e)^{1/4} \sim 0.7\, m_{LH}$. This number becomes larger as the mass ratio increases and would greatly exceed one (i.e., the ion kinetic effects would be negligible) in a realistic ($m_i/m_e = 1836$) case. Indeed, the linear analyses for larger mass ratio cases with $m_i/m_e = 256$ [Fig. 7(g)] and $m_i/m_e = 1836$ [Fig. 7(h)] show that the most unstable modes would be in a range of the pure LHDI without being significantly affected by the ion gyro-motion (i.e., $\alpha_{IC} \gg 1$). Here, the input parameters to the linear dispersion relation solver for these high m_i/m_e cases are set to be the same as the case for Fig. 7(f) except for higher m_i/m_e and corresponding larger ω_{pe}/ω_{ce} and V_{te}/c. An additional simulation for $m_i/m_e = 256$, in which the initial settings are the same as run-B except for smaller L_z ($= 2d_i$) and 1.6 [$= (256/100)^{0.5}$] times smaller grid-spacing, shows that the dominant mode for $m_i/m_e = 256$ is indeed $m_{LH} \sim 3$ [Fig. 7(e)] as predicted from the linear analysis [Fig. 7(g)], supporting the predictions from the linear analyses.

Based on the above consistencies between the simulation and the linear analysis, we further applied the linear dispersion relation solver to real parameters obtained from the MMS observation event treated in this paper and Blasl *et al.* (unpublished). The input parameters, based on the local values near the time interval with large amplitudes

of the field fluctuations at the trailing edge of the KH waves, shown in Fig. 10 in Blasl *et al.* (unpublished) (~15:56 UT), are $m_i/m_e = 1836$, $T_i/T_e = 11.6$, $\omega_{pe}/\omega_{ce} = 21.4$, $V_{di}/V_{ti} = 0$, $V_{de}/V_{te} = 0.12$, $V_{ti}/c = 0.0012$, and $V_{te}/c = 0.015$ ($\beta \sim 2.5$). Figure 7(i) shows the results of the linear analysis for this MMS event. Similar to the above simulation cases, a quasi-perpendicular wave mode with $\phi \sim 87°$ relative to the ambient magnetic field has the maximum growth rate $\gamma \sim 0.2\omega_{LHR}$ at a wave number $k_\perp(\rho_i\rho_e)^{1/2} \sim 3$. This wave number corresponds to $\lambda \sim 56$ km. Given the simulation result that the wavelength of the dominant modes tends to become 1.5–2 times longer as the LHDI develops [see blue curve in Fig. 7(c)], this predicted wavelength of the fastest growing mode is in reasonable agreement with the estimation from the observed field fluctuations in this MMS event (~80–100 km) [see Blasl *et al.* (unpublished) for more details of the MMS observations of the small-scale field fluctuations between the KH waves]. Together with the above quantitative consistencies between the simulation and the MMS event on the large-scale evolution of the primary KHI/RTI shown in Sec. III B, these results naturally suggest that the LHDI-driven turbulence at the edges of the KHI/RTI waves/vortices as seen in the present simulation may occur in the Earth's magnetopause during the southward IMF.

C. Turbulent reconnection

The top panels in Fig. 8 show the B_z component in the x–y plane at $t = 5.4\alpha^{-1}$ (early non-linear growth phase of the KHI) in the 3D case (run-B), the corresponding 2D case (run-C), and the 2D case without the initial in-plane magnetic field (run-D). The initial

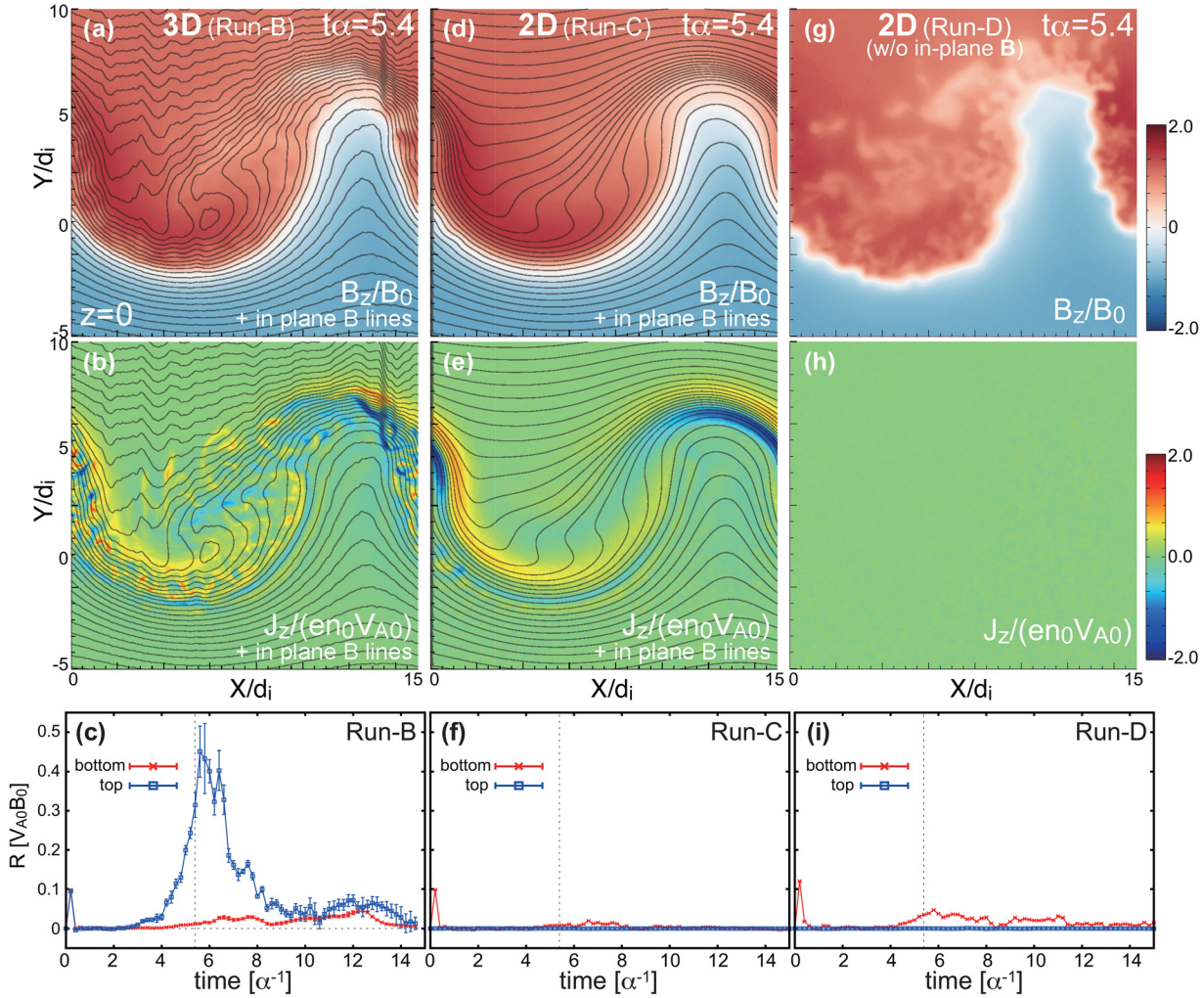

FIG. 8. (Top and middle) Color contours of B_z and J_z at $t = 5.4\alpha^{-1}$ in the x–y plane ($z = 0$ for the 3D run), and (bottom) time evolutions of the normalized, global reconnection rate R (Daughton *et al.*, 2014) computed from the integrated magnetic flux that crosses the mixing surfaces, defined as $|F_e| = 0.99$, on the low-density and positive-B_z (top) and high-density and negative-B_z (bottom) sides for runs-B–D. Here $F_e = (n_{e1} - n_{e2})/(n_{e1} + n_{e2})$ is the mixing measure. The black curves for runs-B and C show the surfaces of the z-component of the vector potential corresponding to the in-plane magnetic field lines in 2D. The vertical lines in the bottom plots indicate the time shown in the top plots.

anti-parallel magnetic field forms the thin primary current layer (corresponding to the density gradient layer) along the edge of the large-scale surface wave in all cases. However, the small-scale fluctuations induced by the LHDI disturb and broaden the upper positive-B_z side (low-density side) of the layer for runs-B and D. Note that for run-C, the in-plane magnetic field, which is locally compressed and enhanced along the edge of the surface wave [see black curves in Fig. 8(d)], prevents the small-scale fluctuations from growing (i.e., the quasi-perpendicular unstable LHDI modes do not exist in the 2D simulation plane), while for run-B, a similar enhancement of the in-plane field is seen but the LHDI can grow obliquely in the direction nearly perpendicular to the magnetic field as shown in Sec. IV C. The middle panels in Fig. 8 show the J_z component for the three runs, while the bottom panels show the time evolution of the global reconnection rate computed from the integrated magnetic flux that crosses the (mixing) surfaces of the layer on the low-density and positive-B_z (top) and the high-density and negative-B_z (bottom) sides (Daughton *et al.*, 2014). For runs-B and C, the compressed in-plane field produces strong out-of-plane currents (J_z) mainly in the low-density side of the primary gradient layer [Figs. 8(b) and 8(e)]. For run-B, the magnetic flux rapidly flows into the low-density side of the primary layer [Fig. 8(c)]. These results indicate that magnetic reconnection occurs within the low-density side of the layer where the strong J_z (i.e., the large magnetic shear) is produced by the compressed in-plane field as mentioned above. Note that since the surfaces of the z-component of the vector potential do not exactly correspond to the in-plane field lines in 3D, the J_z variations for run-B [Fig. 8(b)] are not exactly aligned with the surfaces of the potential [black curves in Fig. 8(b)], especially near the head of the high-density arm where the magnetic field lines are three-dimensionally twisted [Fig. 6(g)]. Note also that we see no significant enhancement of the inflowing flux in the 2D cases [Figs. 8(f) and 8(i)]. This is because the unstable mode of the tearing instability satisfying $\boldsymbol{k} \cdot \boldsymbol{B} = 0$ cannot be found in the 2D simulation planes (i.e., there is no anti-parallel, in-plane component of the magnetic field).

It is notable that the rate of the flux inflow on the high-density side for run-B [see the red curve in Fig. 8(c)] is about ten times smaller than that on the low-density side ($R \sim 0.5$). This indicates that in this 3D case, reconnection occurs mostly on the low-density side and hardly occurs between the two sides across the primary layer (i.e., between the northward and southward magnetic field lines across the magnetopause). This could be because the small-scale fluctuations broaden the low-density side of the layer and prevent the inflowing flux on the low-density side from reaching the high-density side across the layer. This result is not seen in recent 3D fully kinetic simulations in the southward IMF case (Nakamura *et al.*, 2020a), in which the initial density jump is set to be weak ($n_{10}/n_{20} = 3.0$), no significant evolution of the LHDI fluctuations is seen, and reconnection strongly develops across the layer. Note that a weak enhancement of the flux inflow rate on the high-density side is seen not only for run-B but also for run-D in which reconnection cannot occur in the 2D simulation plane [see the red curves in Figs. 8(c) and 8(i)]. These weak enhancements on the high-density side result from the mixing caused by the LHDI fluctuations.

D. Plasma transport and mixing

Figure 9(a) shows the time evolution of the thickness in the boundary normal (y) direction of the region where the profile in the x-direction contains the density variation larger than $0.3(n_{10} - n_{20})$, for runs B–D. This thickness roughly corresponds to the penetration distance of the high-density arm into the low-density side. For all runs, we see a similar continuous penetration of the arm, corresponding to a similar evolution of the large-scale KHI/RTI (see also top panels in Fig. 8), at a speed $0.3–0.4V_0$ until $t \sim 6\alpha^{-1}$. Note that for runs B–D, the penetration is suppressed at $t \sim 6\alpha^{-1}$ by the effects of the simulation boundaries in the y-direction, while for run-A, in which the system size is set to be larger than that for runs B–D, the penetration continues even after $t \sim 6\alpha^{-1}$ without being affected by the boundaries [see the black curve in Fig. 9(a)].

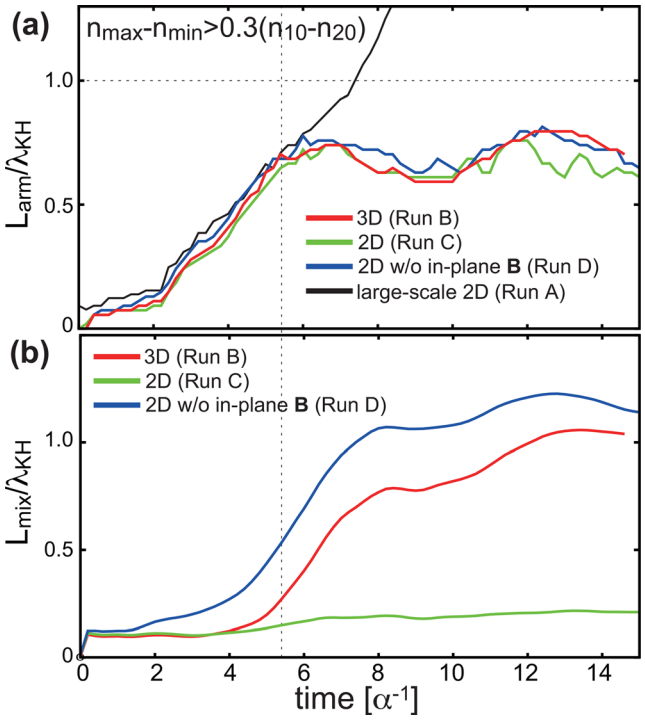

FIG. 9. Time evolutions of (a) the length in the boundary normal (y) direction of the region with the large-scale density fluctuations (i.e., the high-density arm), defined as the region where the profile in the x-direction contains the density variation larger than $0.3(n_{10} - n_{20})$, and (b) the averaged thickness in y of the mixing region with $|F_e| < 0.99$ for runs B–D. The black curve in (a) shows the result from run-A in which the normalized units λ_{KH} and $\alpha^{-1} = \lambda_{KH}/V_0$ are employed for the fastest growing mode $m_x = 6$. The vertical lines in (a) and (b) indicate the time shown in Fig. 8.

Figure 9(b) shows the time evolution of the averaged thickness in the y direction of the mixing region defined as the region with $|F_e| < 0.99$ for runs B–D. We clearly see that for runs-B and D, in which the LHDI turbulence occurs, the mixing region expands much more efficiently than run-C. This indicates that the LHDI turbulence dominantly contributes to the mixing between the high- and low-density sides in the vortex layer, while the RTI and the resulting penetration of the high-density arm, which contribute to the convective transport of high-density plasmas into the low-density side as shown in Fig. 9(a), do not significantly contribute to the plasma mixing between the two sides.

E. Detection probability of the primary KH mode

Similar evolutions of the high-density arm for all runs shown in Fig. 9(a) indicate that the local mixing by the LHDI turbulence does not significantly disturb the large-scale evolution of the KHI and RTI—i.e., the primary KHI and the subsequent secondary RTI are the dominant processes to control the large-scale evolution of the shear layer. As described in Sec. IV A, during this large-scale evolution of the layer, the high-density arm becomes narrower as the arm develops in the boundary normal direction. This suggests that when the spacecraft crosses the vortex layer, the observed dominant mode would be different at different locations (relative to the high-density arm) and/or at different times (depending on the growth phases of the KHI and RTI). Figures 10(a) and 10(b) show k_x spectra for run-B of the total pressure for each y (corresponding to the spectra from the virtual observations in which the virtual probe crosses the layer in the x direction at each y) at $t = 3\alpha^{-1}$ and $t = 6\alpha^{-1}$ (before and after the onset of the RTI). At $t = 3\alpha^{-1}$, a dominant mode of the KHI ($m_x = 1$) is clearly seen near $y \sim 0$, while at $t = 6\alpha^{-1}$, smaller-scale modes become visibly stronger especially at the low-density side ($y > 0$) and it is no longer easy to identify one dominant mode. Notice that this flattening of the spectra corresponds to the formation of intermittent and irregular variation patterns of the surface waves as shown in Figs. 3(a)–3(h) for run-A.

Figures 10(c) and 10(d) show the k_x spectra integrated over y of the total pressure and the y component of the ion bulk velocity. At $t = 3\alpha^{-1}$, the amplitude of the primary KH ($m_x = 1$) mode is more than one order of magnitude larger than that of the smaller-scale modes, while at $t = 6\alpha^{-1}$ and later times, the difference in the amplitude between the KHI and smaller-scale modes becomes much smaller. Figure 10(f) shows the time evolution of the ratio of the amplitude of the primary KH ($m_x = 1$) mode and the smaller-scale

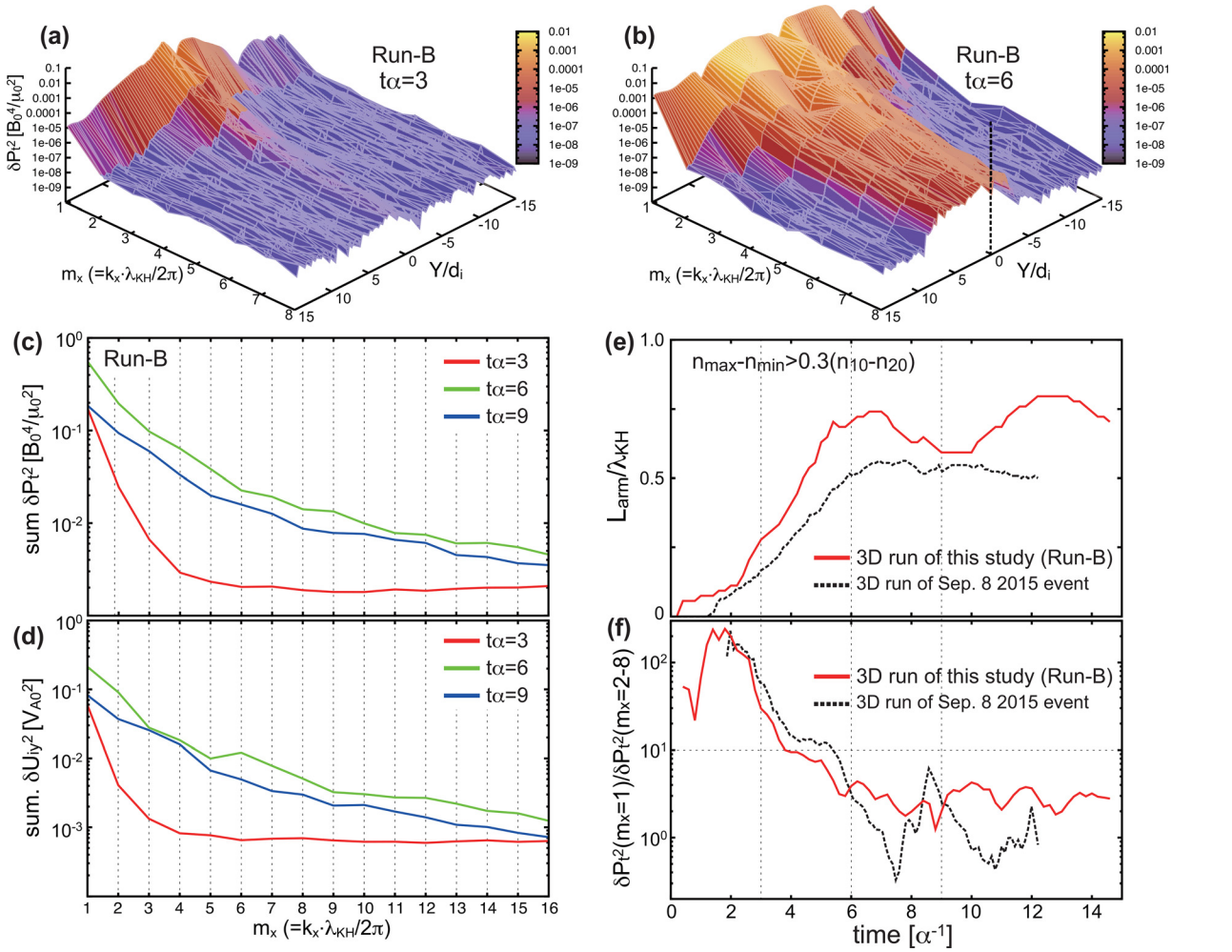

FIG. 10. [(a) and (b)] 1D power spectra (k_x) for run-B of the total pressure P_t for each y averaged in z at $t = 3\alpha^{-1}$ (linear phase) and $t = 6\alpha^{-1}$ (early non-linear phase). [(c) and (d)] The same spectra as (a) and (b) but integrated in y of (c) P_t and (d) U_{iy} at $t = 3$, 6, and $9\alpha^{-1}$. [(e) and (f)] Time evolution for run-B of (e) the thickness of the region with the large-scale density fluctuations [the same as the red curve in Fig. 9(a)], and (f) the ratio of the P_t power between $m_x = 1$ and $m_x = 2$–8 within the region having the moderate density fluctuations. The black dashed curves in (e) and (f) show the results calculated from the 3D run of the September 8, 2015 event employed in Nakamura (2021), in which the KH waves were observed during northward IMF.

($m_x = 2–8$) modes. The ratio becomes below 10 (i.e., the amplitudes of the primary KH and smaller scale modes become within an order of magnitude) at $t \sim 3.5–4\alpha^{-1}$, indicating that it quickly becomes difficult to identify the primary KH mode just after the onset of the secondary RTI ($t \sim 3\alpha^{-1}$). As shown in Fig. 10(e) [the same as the red curve in Fig. 9(a)], the decrease in the ratio roughly corresponds to the evolution of the high-density arm. These results may explain the low observational probability of the KH waves during southward IMF periods (e.g., Kavosi and Raeder, 2015)—i.e., during southward IMF, even when the KHI is unstable at the magnetopause, the evolution of the secondary RTI and the resulting penetration of the high-density arm could make it difficult to identify the periodic KH waves.

V. SUMMARY AND DISCUSSION

A. Summary

Based on the 2D and 3D fully kinetic simulations of the MMS event on September 23, 2017, in which signatures of the KH waves were observed during a southward IMF interval as shown in our companion paper Blasl *et al.* (unpublished), we investigated the evolution process of the KH waves and related secondary waves/instabilities during the southward IMF. The main results of this paper are summarized as follows:

1. The KHI is indeed unstable and forms surface waves at the magnetopause boundary layer (velocity shear layer) under the parameters obtained from the MMS observations during southward IMF on September 23, 2017.
2. As the primary KHI grows, the ion current, which is produced by the anti-parallel (south–north) magnetic field across the surface and flows in the direction nearly parallel to the background shear flow (i.e., in the equatorial plane), is bent in the boundary normal direction and drives the secondary RTI.
3. The growth of the RTI results in the penetration of high-density arms into the low-density (magnetospheric) side, which disturbs the vortex motion and significantly reduces the observational probability of the primary KH waves.
4. At the edge of the KH waves and the high-density arms, where the thin density gradient layer forms, the LHDI is induced and produces the small-scale (hybrid kinetic-scale) fluctuations in the perpendicular component of the electric field. The LHDI grows mainly in the low-density side of the gradient layer, leading to the diffusion of the layer.
5. The secondary RTI and the resulting penetration of the high-density arms cause plasma transport into the low-density side, while the LHDI contributes to the plasma mixing along the edge of the primary KH waves and the high-density arms.
6. Although signatures of magnetic reconnection (inflowing magnetic flux) are observed within the LHDI turbulence, reconnection does not significantly grow across the primary shear layer.
7. The large-scale variations of the surface waves by the KHI and RTI and the small-scale fluctuations by the LHDI are reasonably consistent with those seen in the MMS observations [see Blasl *et al.* (unpublished) for details of the MMS observations].

B. IMF dependence

A key difference in the profile across the low-latitude magnetopause between the northward and southward IMF cases is the direction (and the amplitude) of the current produced by the magnetic shear between the magnetosheath and magnetospheric sides compared to the background shear flow (the equatorial plane). During the northward IMF, the magnetopause current is weaker and flows in the direction largely tilted from the shear flow, while during southward IMF, stronger current flows in the direction closer to the shear flow. As shown in Sec. IV A, during southward IMF, this strong in-plane current causes the secondary RTI at the boundary layer bent by the KH waves, leading to the deep penetration of the high-density arm into the magnetospheric side. Here, the ratio of the growth rates of the primary KHI and the secondary RTI can roughly be estimated in the incompressible MHD regime (Chandrasekhar, 1961) as

$$\frac{\gamma_{KH}}{\gamma_{RT}} \sim \sqrt{\frac{(k_{KH}V_0)^2}{k_{RT}(V_{MP}{}^2/r)}} = \sqrt{\frac{r\lambda_{RT}}{\lambda_{KH}{}^2}}\frac{V_0}{V_{MP}},$$

where k_{KH}, k_{RT}, λ_{KH}, and λ_{RT} are the wavenumber and wavelength of the KHI and RTI, respectively, r is the curvature radius of the surface wave, and V_{MP} is the parallel (to the shear flow) velocity component of ions that partly carry the magnetopause current. Assuming that the current is carried only by ions with typical parameters near the flank magnetopause as the layer thickness $L_{MP} \sim 10^3$ km, the magnetic field varying from −20 to 20 nT across the layer (i.e., $\Delta B_z \sim 40$ nT) and the density near the center of the layer $n_{MP} \sim 1\,\mathrm{cm}^{-3}$, V_{MP} is roughly estimated as $V_{MP} \sim (\Delta B_z/L_{MP})/(\mu_0 e n_{MP}) \sim 200$ km/s, which is comparable to the amplitude of the shear flow near the flank magnetopause (i.e., $V_{MP} \sim V_0$). Since λ_{RT} and r, both of which depend on λ_{KH}, are only a few times smaller than λ_{KH} and comparable to λ_{KH}, respectively, as shown in Sec. IV A, the growth rate of the secondary RTI would commonly be comparable to that of the primary KHI at the flank magnetopause. Thus, the strong growth of the RTI and the resulting deep penetration of the high-density arm as seen in the present simulations could actually occur at the flank magnetopause during southward IMF.

The black dashed curves in Figs. 10(e) and 10(f) show the results from the 3D run of an MMS observation event of KH waves during northward IMF on September 8, 2015 (Nakamura *et al.*, 2017a; 2017b; Nakamura, 2021). In this northward IMF case, the vortex-induced reconnection quickly destroys the structure of the primary KH vortex (Nakamura *et al.*, 2017b), leading to the quick decrease in the relative amplitude of the primary KH mode as seen in Fig. 10(f). Interestingly, the decrease rate in the present simulation for southward IMF is somewhat larger than the simulation for northward IMF [compare red solid and black dashed curves in Fig. 10(f)]. This could be because of the quicker evolution of the high-density arm due to the RTI for the southward IMF case [compare red solid and black dashed curves in Fig. 10(e)]. This result indicates that it would be rather difficult to identify the KH waves from the periodicity of the surface waves during southward IMF even when the unstable condition for the KHI is satisfied. In addition, notice that the evolution of the high-density arm for the southward IMF leads to intermittent and irregular variation patterns of the plasma and field parameters as shown in Figs. 3(a)–3(h). Similar variation patterns were observed in the MMS event treated in this paper [see Figs. 3(i)–3(l)] as well as the past observation of the KH waves during southward IMF by Cluster (Hwang *et al.*, 2011). Combined with similar estimated growth rates of the RTI and KHI, the intermittent and irregular variation patterns of the surface waves would be a common feature of KH waves observed during southward IMF.

C. Some remarks on future work

Recent 3D kinetic simulations of the magnetopause KHI showed that reconnection induced by the magnetic shear across the magnetopause quickly decays the non-linear vortex structure for both northward (Nakamura *et al.*, 2017a; 2017b) and southward (Nakamura *et al.*, 2020a) IMF cases. On the other hand, in the present simulation which has a density jump across the magnetopause that is more than two times higher than the jumps employed in these recent simulations, the secondary RTI and LHDI driven by the large density gradient are the main processes that control the non-linear vortex structure, and reconnection occurs only locally within the LHDI turbulence. These results suggest that while reconnection plays a key role in controlling the non-linear KH vortex structure for both northward and southward IMFs if the density jump across the magnetopause is sufficiently small, as the density jump becomes larger, the secondary RTI and LHDI become more active and can play a more significant role in controlling the vortex structure. We expect the density jump to be generally larger for southward IMF conditions when the LLBL is thinner or less prominent than for northward IMF (Mitchell *et al.*, 1987). An additional survey on the density ratio across the magnetopause would lead to a more systematic understanding of the secondary reconnection, RTI and LHDI processes and their dependence on the density ratio across the magnetopause.

In the present 3D simulation, as shown in Sec. IV A, the secondary RTI dominates plasma transport into the low-density side and strongly disturbs the large-scale vortex structure, while as shown in Sec. IV B, the secondary LHDI broadens the low-density side of the density gradient layer where plasmas are mixed across the layer. Assuming that the primary KHI, whose wavelength and phase speed are $\lambda_{KH} \sim 10^{4-5}$ km and $V_{ph} \sim V_0 \sim 200$–300 km/s, respectively, starts growing near the dayside-to-flank magnetopause, since the secondary processes are driven in the non-linear growth phase of the primary KHI, which corresponds to $\Delta x \sim V_0 \cdot 4\alpha^{-1} \sim 4\lambda_{KH} \sim$ a few to 50 Earth radii from the onset location of the primary KHI, the vortex-induced diffusive plasma transport and mixing would be active at the flank-to-tail magnetopause during southward IMF.

However, to more quantitatively understand these diffusive processes, further simulations under more realistic conditions would be required. For example, as shown in Fig. 7, since the growth rate of the LHDI and the related ion-kinetic effects depend on the ion-to-electron mass ratio, to understand the actual roles of the LHDI turbulence (as well as reconnection within the turbulence), larger-scale simulations with higher mass ratios would need to be performed. In addition, although the evolution of the secondary RTI would not be significantly affected by the mass ratio, as shown in Fig. 10(a), the depth that the high-density arm can penetrate into the low-density side depends on the simulation system size. Thus, to estimate the actual transport rate and understand the role of the RTI, larger-scale simulations would also need to be performed. Furthermore, since the pure (i.e., non-KHI-related) reconnection process and related phenomena, such as flux transfer events frequently occur at the low-latitude magnetopause during southward IMF (e.g., Fuselier, 2021 and references therein), to more comprehensively understand the local physics of the KHI, it would also be required to consider the global coupling with the other processes. Although it is difficult to include these global physics in the fully kinetic regime, global hybrid (fluid-electron and kinetic-ions) simulations, which recently became applicable to the whole Earth's magnetosphere (e.g., Palmroth *et al.*, 2018; Guo *et al.*, 2021), may provide important support for treating such global inter-process couplings.

As discussed above, the estimated ion velocity component produced by the magnetopause current V_{MP} (~200 km/s) is close to the background velocity shear across the magnetopause ($V_{MP} \sim V_0$). Although V_{MP} is basically dominant within the current layer and the shearing flow component is less effective within the current layer, the shearing flow can modify the total flow profile to some degree. At the dusk-side magnetopause as in the present MMS event, the direction of the shearing flow is close to that of the ion current, and therefore the shearing flow can enhance the total flow and strengthen the growth of the RTI, while on the dawn-side, the direction of the shearing flow is mostly opposite from the ion current and therefore the RTI can be weakened. This effect would increase with increasing down tail distance, as the velocity shear becomes stronger. Thus, there may be a local-time difference in the plasma transport rate by the KHI/RTI during southward IMF. Systematically surveying the local-time dependence would also be important to more practically understand the effects of the magnetopause KHI during southward IMF.

Finally, it should be noted that the present simulations started from a Harris-type current layer in which the total pressure within the layer is sustained by the plasma pressure and the magnetic field strength within the layer is weaker than that in the background regions. Although no significant decrease in the magnetic field strength near the current layer crossings of this MMS event [for example, see Fig. 3 in Blasl *et al.* (unpublished)] may indicate that the observed KH waves were driven at a non-Harris-type layer, it is difficult to know the exact initial equilibrium conditions from the observations. Past observational and analytical studies of the Earth's magnetopause crossings showed that in addition to the Harris-type layer, the force-free configuration of the current layer, in which the magnetic field strength is nearly constant across the layer, also exists at the magnetopause (Panov *et al.*, 2011). Investigating these different types of the initial current layers would be required to more systematically understand the evolution process of the magnetopause KH waves during southward IMF.

VI. CONCLUSIONS

We have performed a series of 2D and 3D fully kinetic simulations of an MMS observation event on September 23, 2017 in which the KH waves were observed at the dusk-flank magnetopause during southward IMF. This is the first numerical challenge to investigate the magnetopause KHI under realistic parameters for the southward IMF. The simulations demonstrate (i) that the KHI is unstable under the parameters of this MMS event; (ii) that the growth of the secondary RTI and the subsequent penetration of high-density arms into the low-density side disturb the primary vortex structure and produce intermittent and irregular variations of the surface waves, leading to a low observational probability of the primary KH waves; and (iii) that the secondary LHDI induced near the vortex edge causes the efficient plasma mixing across the magnetopause. The large-scale variations of the surface waves and the small-scale fluctuations from the LHDI are reasonably consistent with the MMS observations. These results indicate that the multi-scale secondary processes and the resulting plasma transport and mixing as shown in the present simulations may actually occur at the flank-to-tail magnetopause during southward IMF.

ACKNOWLEDGMENTS

This work was supported by the Austrian Research Fund (FWF) (No. P32175-N27). For the simulations employed in this paper, we acknowledge PRACE for awarding us access to MareNostrum at Barcelona Supercomputing Center (BSC), Spain. A part of the simulation data were analyzed with resources at the Space Research Institute of Austrian Academy of Sciences. The observation data employed in this paper were obtained from the MMS spacecraft and are publically available via NASA resources and the Science Data Center at CU/LASP (https://lasp.colorado.edu/mms/sdc/public/). The work by H.H. was supported by JSPS Grant-in-aid for Scientific Research KAKENHI JP21K03504. J.E.S. was supported by the Royal Society University Research Fellowship (No. URF\R1\201286). The work by T.U. was supported by JSPS Grant-in-aid for Scientific Research KAKENHI JP19H01868. Y.-H.L. and S.A.P. are grateful for support from grants NSF-DoE 1902867 and NASA MMS 80NSSC18K0289.

AUTHOR DECLARATIONS

Conflict of Interest

The authors declare that the research was conducted in the absence of any commercial or financial relationships that could be construed as a potential conflict of interest.

DATA AVAILABILITY

The data that support the findings of this study are openly available in Zenodo at https://doi.org/10.5281/zenodo.5725490 [Nakamura (2021)].

REFERENCES

Blasl, K. A., Nakamura, T. K. M., Plaschke, F., Nakamura, R., Hasegawa, H., Stawarz, J. E., Liu, Y.-H., Peery, S. A., Holmes, J. C., Hosner, M., Schmid, D., Roberts, O. W., and Volwerk, M., "Multi-scale observations of the magnetopause Kelvin-Helmholtz waves during southward IMF," Phys. Plasmas **29**, 012105 (2022).

Bowers, K. J., Albright, B. J., Yin, L., Bergen, B., and Kwan, T. J. T., "Ultrahigh performance three-dimensional electromagnetic relativistic kinetic plasma simulation," Phys. Plasmas **15**, 055703 (2008).

Bowers, K. J., Albright, B. J., Yin, L., Daughton, W., Roytershteyn, V., Bergen, B., and Kwan, T. J. T., "Advances in petascale kinetic simulations with VPIC and roadrunner," J. Phys.: Conf. Ser. **180**, 012055 (2009).

Burch, J. L., Moore, T. E., Torbert, R. B., and Giles, B. L., "Magnetospheric multiscale overview and science objectives," Space Sci. Rev **199**, 5–21 (2016).

Cassak, P. A. and Otto, A., "Scaling of the magnetic reconnection rate with symmetric shear flow," Phys. Plasmas **18**, 074501 (2011).

Chandrasekhar, S., *Hydrodynamic and Hydromagnetic Stability* (Oxford University Press, New York, 1961).

Daughton, W., "Electromagnetic properties of the lower-hybrid drift instability in a thin current sheet," Phys. Plasmas **10**, 3103 (2003).

Daughton, W., Nakamura, T. K. M., Karimabadi, H., Roytershteyn, V., and Loring, B., "Computing the reconnection rate in turbulent kinetic layers by using electron mixing to identify topology," Phys. Plasmas **21**, 052307 (2014).

Davidson, R. C., Gladd, N. T., Wu, C. S., and Huba, J. D., "Effects of finite plasma beta on the lower-hybrid-drift instability," Phys. Fluids **20**, 301–310 (1977).

Eriksson, S., Lavraud, B., Wilder, F. D., Stawarz, J. E., Giles, B. L., Burch, J. L., Baumjohann, W., Ergun, R. E., Lindqvist, P.-A., Magnes, W. *et al.*, "Magnetospheric multiscale observations of magnetic reconnection associated with Kelvin-Helmholtz waves," Geophys. Res. Lett. **43**, 5606–5615, https://doi.org/10.1002/2016GL068783 (2016a).

Eriksson, S., Wilder, F. D., Ergun, R. E., Schwartz, S. J., Cassak, P. A., Burch, J. L., Chen, L.-J., Torbert, R. B., Phan, T. D., Lavraud, B. *et al.*, "Magnetospheric multiscale observations of the electron diffusion region of large guide field magnetic reconnection," Phys. Rev. Lett. **117**, 015001 (2016b).

Fairfield, D. H., Otto, A., Mukai, T., Kokubun, S., Lepping, R. P., Steinberg, J. T., Lazarus, A. J., and Yamamoto, T., "Geotail observations of Kelvin-Helmholtz instability at the equatorial magnetotail boundary for parallel northward fields," J. Geophys. Res. **105**, 21159, https://doi.org/10.1029/1999JA000316 (2000).

Fairfield, D. H., Kuznetsova, M. M., Mukai, T., Nagai, T., Gombosi, T. I., and Ridley, A. J., "Waves on the dusk flank boundary layer during very northward interplanetary magnetic field conditions: Observations and simulation," J. Geophys. Res. **112**, A08206, https://doi.org/10.1029/2020JA028670 (2007).

Foullon, C., Farrugia, C. J., Fazakerley, A. N., Owen, C. J., Gratton, F. T., and Torbert, R. B., "Evolution of Kelvin-Helmholtz activity on the dusk flank magnetopause," J. Geophys. Res. **113**, A11203, https://doi.org/10.1029/2008JA013175 (2008).

Fuselier, S. A., "Dayside magnetopause processes," in *Magnetospheres in the Solar System*, edited by R. Maggiolo, N. André, H. Hasegawa, D. T. Welling, Y. Zhang and L. J. Paxton (Wiley, 2021).

Guo, J., Lu, S., Lu, Q., Lin, Y., Wang, X., Huang, K., Wang, R., and Wang, S., "Structure and coalescence of magnetopause flux ropes and their dependence on IMF clock angle: Three-dimensional global hybrid simulations," J. Geophys. Res.: Space Phys. **126**, e2020JA028670, https://doi.org/10.1029/2020JA028670 (2021).

Hasegawa, H., Fujimoto, M., Phan, T.-D., Rème, H., Balogh, A., Dunlop, M. W., Hashimoto, C., and TanDokoro, R., "Transport of solar wind into Earth's magnetosphere through rolled-up Kelvin-Helmholtz vortices," Nature **430**, 755 (2004).

Hasegawa, H., Fujimoto, M., Takagi, K., Saito, Y., Mukai, T., and Rème, H., "Single-spacecraft detection of rolled-up Kelvin-Helmholtz vortices at the flank magnetopause," J. Geophys. Res. **111**, A09203, https://doi.org/10.1029/2006JA011728 (2006).

Hasegawa, H., Nakamura, T. K. M., Gershman, D. J., Nariyuki, Y., Viñas, A. F., Giles, B. L., Lavraud, B., Russell, C. T., Khotyaintsev, Y. V., Ergun, R. E., and Saito, Y., "Generation of turbulence in Kelvin-Helmholtz vortices at the Earth's magnetopause: Magnetospheric Multiscale observations," J. Geophys. Res.: Space Phys. **125**, e2019JA027595, https://doi.org/10.1029/2019JA027595 (2020).

Hwang, K.-J., Kuznetsova, M. M., Sahraoui, F., Goldstein, M. L., Lee, E., and Parks, G. K., "Kelvin-Helmholtz waves under southward interplanetary magnetic field," J. Geophys. Res. **116**, A08210, https://doi.org/10.1029/2011JA016596 (2011).

Hwang, K. J., Dokgo, K., Choi, E., Burch, J. L., Sibeck, D. G., Giles, B. L., Hasegawa, H., Fu, H. S., Liu, Y., Wang, Z., Nakamura, T. K. M. *et al.*, "Magnetic reconnection inside a flux rope induced by Kelvin-Helmholtz vortices," J. Geophys. Res.: Space Phys. **125**, e2019JA027665, https://doi.org/10.1029/2019JA027665 (2020).

Kavosi, S. and Raeder, J., "Ubiquity of Kelvin–Helmholtz waves at Earth's magnetopause," Nat. Commun. **6**, 7019 (2015).

Kokubun, S., Kawano, H., Nakamura, M., Yamamoto, T., Tsuruda, K., Hayakawa, H., Matsuoka, A., and Frank, L. A., "Quasi-periodic oscillations of the magnetopause during northward sheath magnetic field," Geophys. Res. Lett. **21**, 2883–2886, https://doi.org/10.1029/94GL02103 (1994).

Kieokaew, R., Lavraud, B., Foullon, C., Toledo-Redondo, S., Fargette, N., Hwang, K.-J., Malakit, K., Ruffolo, D., Øieroset, M., T.-D. Phan *et al.*, "Magnetic reconnection inside a flux transfer event-like structure in magnetopause Kelvin-Helmholtz waves," J. Geophys. Res.: Space Phys. **125**, e2019JA027527, https://doi.org/10.1029/2019JA027527 (2020).

Kivelson, M. G. and Chen, S.-H., "The magnetopause: Surface waves and instabilities and their possible dynamic consequences," in *Physics of the Magnetopause*, Geophysical Monograph Series, edited by P. Song *et al.* (AGU, Washington, DC, 1995), Vol. 90.

Li, W., André, M., Khotyaintsev, Y. V., Vaivads, A., Graham, D. B., Toledo-Redondo, S., Norgren, C., Henri, P., Wang, C., Tang, B. B. *et al.*, "Kinetic evidence of magnetic reconnection due to Kelvin-Helmholtz waves," Geophys. Res. Lett. **43**, 5635–5643, https://doi.org/10.1002/2016GL069192 (2016).

Mitchell, D. G., Kutchko, F., Williams, D. J., Eastman, T. E., Frank, L. A., and Russell, C. T., "An extended study of the low-latitude boundary layer on the dawn and dusk flank of the magnetosphere," J. Geophys. Res. **92**(A7), 7394–7404, https://doi.org/10.1029/JA092iA07p07394 (1987).

Moore, T. W., Nykyri, K., and Dimmock, A. P., "Cross-scale energy transport in space plasmas," Nat. Phys. **12**, 1164–1169 (2016).

Nakamura, T. K. M., Fujimoto, M., and Otto, A., "Structure of an MHD-scale Kelvin-Helmholtz vortex: Two-dimensional two-fluid simulations including finite electron inertial effects," J. Geophys. Res. **113**, A09204, https://doi.org/10.1029/2007JA012803 (2008).

Nakamura, T. K. M., Daughton, W., Karimabadi, H., and Eriksson, S., "Three-dimensional dynamics of vortex-induced reconnection and comparison with THEMIS observations," J. Geophys. Res. **118**, 5742–5757, https://doi.org/10.1002/jgra.50547 (2013).

Nakamura, T. K. M. and Daughton, W., "Turbulent plasma transport across the Earth's low-latitude boundary layer," Geophys. Res. Lett. **41**, 8704–8712, https://doi.org/10.1002/2014GL061952 (2014).

Nakamura, T. K. M., Hasegawa, H., Daughton, W., Eriksson, S., Li, W. Y., and Nakamura, R., "Turbulent mass transfer caused by vortex-induced reconnection in collisionless magnetospheric plasmas," Nat. Commun. **8**, 1582 (2017a).

Nakamura, T. K. M., Eriksson, S., Hasegawa, H., Zenitani, S., Li, W. Y., Genestreti, K. J., Nakamura, R., and Daughton, W., "Mass and energy transfer across the Earth's magnetopause caused by vortex-induced reconnection," J. Geophys. Res.: Space Phys. **122**(11), 11,505–11,522, https://doi.org/10.1002/2017JA024346 (2017b).

Nakamura, T. K. M., Plaschke, F., Hasegawa, H., Liu, Y. H., Hwang, K. J., Blasl, K. A., and Nakamura, R., "Decay of Kelvin-Helmholtz vortices at the Earth's magnetopause under pure southward IMF conditions," Geophys. Res. Lett. **47**, e2020GL087574, https://doi.org/10.1029/2020GL087574 (2020a).

Nakamura, T. K. M., Stawarz, J. E., Hasegawa, H., Narita, Y., Franci, L., Wilder, F. D., Nakamura, R., and Nystrom, W. D., "Effects of fluctuating magnetic field on the growth of the Kelvin-Helmholtz instability at the Earth's magnetopause," J. Geophys. Res.: Space Phys. **125**, e2019JA027515, https://doi.org/10.1029/2019JA027515 (2020b).

Nakamura, T. K. M., "The Earth's low-latitude boundary layer," in *Magnetospheres in the Solar System*, edited by R. Maggiolo, N. André, H. Hasegawa, D. T. Welling, Y. Zhang, and L. J. Paxton (Wiley, 2021).

Nakamura, T. K. M. (2021). "PIC simulation results of an MMS southward IMF KH wave event," Zenodo. https://doi.org/10.5281/zenodo.5725490

Panov, E. V., Artemyev, A. V., Nakamura, R., and Baumjohann, W., "Two types of tangential magnetopause current sheets: Cluster observations and theory," J. Geophys. Res. **116**, A12204, https://doi.org/10.1029/2011JA016860 (2011).

Palmroth, M., Ganse, U., Pfau-Kempf, Y., Battarbee, M., Turc, L., Brito, T., Grandin, M., Hoilijoki, S., Sandroos, A., and von Alfthan, S., "Vlasov methods in space physics and astrophysics," Living Rev. Comput. Astrophys. **4**, 1 (2018).

Sckopke, N. G., Paschmann, G., Haerendel, G., Sonnerup, B. U. O., Bame, S. J., Forbes, T. G., Hones, E. W., Jr., and Russell, C. T., "Structure of the lowlatitude boundary layer," J. Geophys. Res. **86**, 2099–2110, https://doi.org/10.1029/JA086iA04p02099 (1981).

Slinker, S. P., Fedder, J. A., Sibeck, D. G., Lyon, J. G., Frank, L. A., and Mukai, T., "Simulation of magnetopause oscillations observed January 9, 1996," Geophys. Res. Lett. **30**(11), 1569, https://doi.org/10.1029/2003GL017063 (2003).

Stawarz, J. E., Eriksson, S., Wilder, F. D., Ergun, R. E., Schwartz, S. J., Pouquet, A., Burch, J. L., Giles, B. L., Khotyaintsev, Y., Contel, O. L. *et al.*, "Observations of turbulence in a Kelvin-Helmholtz event on 8 September 2015 by the Magnetospheric Multiscale mission," J. Geophys. Res.: Space Phys. **121**, 11,021–11,034, https://doi.org/10.1002/2016JA023458 (2016).

Tang, B., Li, W., Wang, C., Dai, L., Khotyaintsev, Y., Lindqvist, P.-A., Ergun, R., Le Contel, O., Pollock, C., Russell, C., and Burch, J., "Magnetic depression and electron transport in an ion-scale flux rope associated with Kelvin–Helmholtz waves," Ann. Geophys. **36**, 879–889 (2018).

Umeda, T. and Nakamura, T. K. M., "Electromagnetic linear dispersion relation for plasma with a drift across magnetic field revisited," Phys. Plasmas **25**, 102109 (2018).

Vernisse, Y., B. Lavraud, S. Eriksson, D. J. Gershman, J. Dorelli, C. Pollock, B. Giles, N. Aunai, L. Avanov, J. Burch. *et al.*, "Signatures of complex magnetic topologies from multiple reconnection sites induced by Kelvin-Helmholtz instability," J. Geophys. Res. **121**, 9926, https://doi.org/10.1002/2016JA023051 (2016).